Acta Astronautica 246 (2026) 422–443

Contents lists available at ScienceDirect

Acta Astronautica

journal homepage: www.elsevier.com/locate/actaastro

Research paper

Experimental and numerical studies on the folding and deployment behavior of space deployable wrapped-rib antennas

Shiran Zhu [a,1], Ruiwen Guo [b,c,1], Haochen Liu [a], Xin Jin [c], Xiaofei Ma [c], Jinxiong Zhou [b], Ning An [a,d,*]

[a] Robotic Satellite Key Laboratory of Sichuan Province, Key Laboratory of Advanced Spatial Mechanism and Intelligent Spacecraft, Ministry of Education, School of Aeronautics and Astronautics, Sichuan University, Chengdu 610065, People's Republic of China
[b] State Key Laboratory for Strength and Vibration of Mechanical Structures and School of Aerospace, Xi'an Jiaotong University, Xi'an 710049, People's Republic of China
[c] Xi'an Institute of Space Radio Technology, Xi'an 710100, People's Republic of China
[d] Department of Civil, Environmental and Mechanical Engineering, University of Trento, Trento, 38123, Italy

ARTICLE INFO

Dataset link: https://github.com/SCU-An-Group/Wrapped-rib-Antenna

Keywords:
Deployable structures
Deployment dynamics
Composite thin-walled lenticular booms
Wrappable ribs
Mesh reflector

ABSTRACT

The wrapped-rib antenna is a promising type of deployable structure designed for space missions. It integrates several flexible ribs with a mesh reflector to create a compact mechanism capable of efficient folding and self-deployment. This study integrates experimental and numerical methods to investigate the folding and deployment behaviors of such antennas. A 0.6-meter aperture antenna prototype with a focal length of 165 mm was fabricated with 16 parabolic ribs featuring C-shaped cross-sections and a stretchable fabric/metallic mesh reflector. Experimental tests were carried out to quantify the wrapping moment under quasi-static folding conditions and to record the deployment dynamics through high-speed imaging. Finite element models (FEM) were developed to analyze rib deformation, reflector behavior, and their interactive contact phenomena throughout the process. Additionally, a larger antenna with a diameter of 4 meters and a focal length of 1.1 meters was designed and demonstrated with FEM using composite thin-walled lenticular booms as flexible ribs and a metallic mesh reflector. The folding and deployment performance of this scaled design was thoroughly evaluated via finite element analysis. The results provide critical insights into the folding and deployment mechanics of wrapped-rib antennas, supporting their efficient design in future developments.

1. Introduction

Space antennas are essential for facilitating reliable communication by transmitting and receiving electromagnetic waves, enabling efficient satellite-based communication across global networks [1,2]. Self-deployable antennas have gained significant attention in satellite applications due to their advantages of low weight, high packaging efficiency, and self-deployment capabilities [3–5]. These antennas are particularly suitable for space missions, where compact stowage and reliable passive deployment are essential. Over the years, numerous self-deployable antenna designs have been proposed and analyzed by both industry and academia, highlighting their critical role in modern satellite systems. To achieve high packaging efficiency, most self-deployable antennas incorporate thin-walled composite structures as flexible ribs and reflectors [6–10]. The geometry of these components is carefully designed to facilitate compact folding and safe deployment, minimizing the risk of material failure or plastic deformation while ensuring sufficient structural stiffness in the deployed configuration [11–14]. In recent years, Urata et al. [15] developed a compact Circularly Polarized SAR C-band antenna system for small spacecrafts, featuring a lightweight deployable parabolic mesh reflector with a 3.6-meter diameter and surface accuracy of 3.86 mm. The antenna utilizes 24 flexible steel ribs and metallic mesh reflectors, designed for operation at low Earth orbital altitudes. Oxford Space Systems Ltd (OSS) [16], a UK-based company, specializes in the development of space antennas and structures. The company has filed patents for a deployable wrapped rib assembly design, and based on this, OSS developed a 2.7 m diameter deployable antenna weighing 7 kg with a height of 0.91 m, achieving RMS surface accuracy better than 0.6 mm in the X-band. When stowed, the antenna's dimensions are compact — 0.45 m in length, 0.45 m in width, and 0.05 m in height — and features 48 flexible ribs made

* Corresponding author at: Robotic Satellite Key Laboratory of Sichuan Province, Key Laboratory of Advanced Spatial Mechanism and Intelligent Spacecraft, Ministry of Education, School of Aeronautics and Astronautics, Sichuan University, Chengdu 610065, People's Republic of China.
E-mail address: anning@scu.edu.cn (N. An).
[1] These authors contributed equally to this study.

https://doi.org/10.1016/j.actaastro.2026.04.032
Received 17 November 2025; Received in revised form 20 February 2026; Accepted 13 April 2026
Available online 16 April 2026

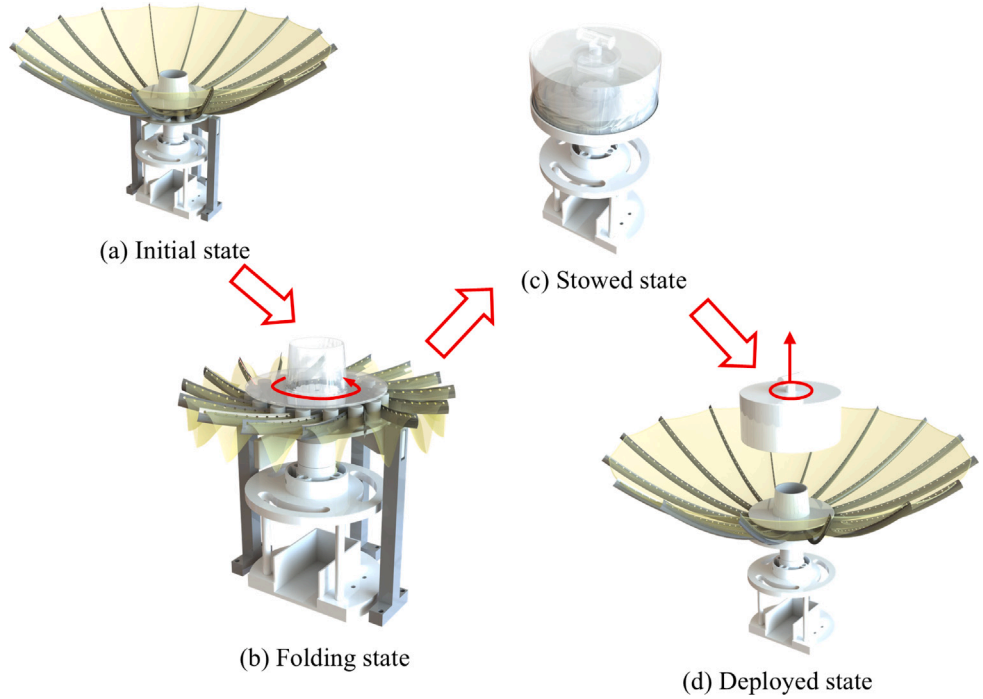

Fig. 1. Schematics of the wrapped-rib antenna in (a) the initial, (b) folding, (c) stowed, and (d) deployed states.

of composite thin-walled lenticular booms with metallic mesh reflectors. Wu et al. [17,18] developed an ultra-compact X-band deployable wrap-rib antenna, featuring 16 stainless steel wrap-ribs and a metallic mesh reflector. They employed form-finding analysis and a genetic algorithm to optimize the rib shape and enhance surface accuracy. Validation tests confirmed the antenna's efficient deployment, stable surface accuracy, and overall performance, positioning it as a promising solution for small-aperture, high-storage-ratio deployable antennas. Lopatin et al. [19] proposed a novel umbrella-type reflector with a transformable rim made of thin-walled composite tape-spring hinges that store elastic energy to deploy lattice spokes via a synchronized Cardan system supporting a reflective mesh.

As a specific type of self-deployable antenna, the wrapped-rib antenna typically consists of multiple flexible parabolic ribs that support a metallic mesh membrane reflector. Fig. 1 schematically illustrates the folding, stowage, and deployment processes of the antenna. During folding, the ribs are wrapped around a central hub. The reflector, made of stainless steel mesh, behaves as a membrane structure with negligible bending stiffness and relies entirely on tensile forces for shape retention. As the ribs deform during folding, the reflector naturally conforms to their shape due to its flexibility. Once folded, the stowed configuration is secured using locking mechanisms, allowing the antenna to be safely transported into orbit by a launch vehicle. Upon arrival in space, these locking mechanisms are released, and the stored strain energy in the ribs drives their autonomous deployment. Simultaneously, the reflector unfolds, becomes tensioned, and is supported by the fully deployed ribs, enabling the antenna to perform its communication functions. Understanding the folding, stowage, and deployment processes of wrapped-rib antennas is therefore essential for optimizing their structural design, operational reliability, and overall performance. This involves careful examination of several key aspects, including the behavior of the flexible ribs and membrane reflector during folding and deployment, and, critically, the interactions between them.

The first major challenge lies in understanding the folding and deployment behavior of flexible ribs [20–22]. In the past, spaceborne deployable antennas like the MARSIS antenna aboard Mars Express [23] and the RIME antenna on ESA's JUICE mission [24] have encountered difficulties during in-orbit deployment. These experiences highlight the importance of closely examining the folding and deployment behavior of flexible ribs. While many studies have investigated the folding and deployment behaviors of thin-walled deployable booms, most existing research has focused on individual straight booms [25]. In contrast, the simultaneous folding and deployment of multiple booms remain largely unexplored, particularly in the case of booms with parabolic curvature. Chu et al. [26] proposed a retractable/deployable mechanism driven by a motor and coupled with reactive springs to facilitate the folding of a space probe for a microsatellite. Lim et al. [27] developed a compact parabolic deployable mesh antenna using superelastic SMA ribs and composite tape springs, and validated its hingeless deployment system through SMA rib tests, deployment trials, surface-error measurements, and finite element simulations. Liu et al. [28] investigated the folding behavior of thin-walled tubular deployable composite booms (DCBs) via experiments and finite element analysis, using custom-designed mechanisms to test folding performance and compare results under Tsai–Hill and maximum stress criteria. Chen et al. [29,30] developed a test setup incorporating a scroll tube and guide wheel to conduct wrapping experiments on composite thin-walled lenticular tube (CTLT) booms, measuring strain and wrapping moments. Bai et al. [31] designed and manufactured a coiling machine consisting of a central driving roller, several constraint shafts, torque sensors, and frame structures. This system can drive and record the flattening and coiling deformations of CTLT booms. Through a combination of experiments and simulations, they also investigated the flattening and wrapping behavior of the lenticular cross-section. More recently, Guo et al. [32] explored the deployment dynamics of CTLTs for space applications by fabricating a two-meter-long CTLT prototype and building a gravity compensation system. Additionally, a high-fidelity numerical model using explicit dynamic finite element

analysis was developed for simulating both the quasi-static folding behavior and the dynamic deployment behavior of CTLTs [33], with good agreement with experimental results. Yan and Wu [34] studied the non-uniform wrapping process of tape springs and developed a theoretical model to predict their wrapping behavior. Their experiments and simulations revealed that the final coiled shape of the tape spring, either polygonal or continuous, is primarily influenced by the radius of the central cylindrical hub. More recently, Liu et al. [35] investigated the dynamic uncoiling of multiple tape springs coiled around a central hub and highlighted the role of inter-member contact during both folding and deployment. However, the tape springs considered were straight members, and coupled rib–membrane interactions were not addressed. In wrapped-rib antennas, by contrast, the ribs are parabolically curved, and this geometry has received limited attention in the folding/deployment literature. Folding and deploying such antennas not only involves simultaneously coiling/uncoiling multiple ribs around a central hub, which inevitably introduces inter-rib contact, but also requires accounting for rib–membrane interactions throughout the process. These coupled effects govern both the stowed configuration and the deployment transient, and remain insufficiently documented compared with rib-only studies that primarily consider isolated ribs/booms.

Another significant challenge lies in analyzing the folding and deployment behavior of membrane reflectors [36]. Membrane-based systems — such as mesh reflectors, solar sails, and inflatable structures — exhibit fundamentally different mechanical characteristics compared to flexible structural elements like composite booms or ribs. As typical tensile structures, membranes are governed by geometric nonlinearity and experience large deformations, leading to a strong coupling between shape evolution and internal stress distribution [37,38]. This coupling presents substantial difficulties for both analytical and numerical modeling. During deployment, the membrane transitions from a stress-free to a tensioned state, significantly altering its effective stiffness and internal force distribution. Accurately simulating such behaviors necessitates advanced numerical methods, typically relying on finite element analysis (FEA) or multi-body dynamics approaches to capture the inherent nonlinearities and coupled interactions. Cai et al. [39] used ABAQUS to simulate the deployment of membrane structures based on the Miura-ori pattern, incorporating a variable Poisson's ratio model to adjust the stress distribution. Xie et al. [40] proposed a roll-out membrane antenna (ROMA) based on thin-walled deployable composite booms (DCBs), highlighting their high deployment-to-package ratio and elastic self-deployment. Numerical simulations and ground tests validated the design, and the successful deployment of the AIS/VDE ROMA on the Pujiang-2 satellite demonstrated the practical significance of thin-walled DCBs in aerospace applications. Saito et al. [41] developed a FEM dynamic simulation to visualize deployment behaviors of thin membranes in space, demonstrating its applicability for drag sails used in de-orbiting artificial structures, with simulation results aligning closely with ground test observations. Yuan et al. [42] developed a dynamic modeling approach for foldable origami space membranes, considering contact-impact during deployment. Using the Absolute Nodal Coordinate Formulation (ANCF) and the Stiffness Reduction Model (SRM), they introduced a mixed method combining surface-to-surface and node-to-surface contact elements to prevent mutual penetration. Despite progress in modeling membrane deployment, most existing studies employ prescribed motions or idealized constraints, such that the evolving load transfer and contact between the membrane and its supporting ribs/booms are not explicitly resolved during the deployment transient. This limitation is particularly relevant for wrapped-rib antennas, where rib–membrane interaction during both wrapping and rapid deployment governs membrane tensioning, stress redistribution, and deployment stability. Form-finding studies, on the other hand, although they consider rib–membrane interaction [17,38], primarily address the deployed equilibrium state to establish the surface figure/accuracy and prestress, rather than the process mechanics of wrapping and rapid deployment. Consequently, systematic studies that capture and validate these coupled process mechanics remain limited, motivating the integrated experimental–numerical investigation adopted in this work.

The analysis of the folding and deployment behavior of wrapped-rib antennas requires focused investigation of several key aspects, including the quasi-static folding mechanics of multiple flexible parabolic ribs, the deployment dynamics of both the ribs and the reflector, and the complex contact interactions among these components throughout the deployment process. Despite the importance of these issues, existing studies typically address the folding and deployment of deployable ribs and membrane reflectors in isolation, without capturing their coupled mechanical behavior. Although rib-reflector interaction is considered in form-finding studies, such work primarily addresses the deployed equilibrium state with the goal of surface-accuracy analysis and optimization, rather than the rib-reflector interactions that govern the folding (wrapping) process and, in particular, the dynamic deployment transient. The main contribution of the present work is the integration of a dedicated experimental setup and finite element simulations to systematically investigate the quasi-static folding and dynamic deployment behavior of a wrapped-rib antenna system, with particular emphasis on the mechanics of multiple flexible ribs, the membrane reflector, and their mutual interactions during both folding and deployment phases. Experiments and simulations were conducted on a 0.6-meter-aperture prototype wrapped-rib antenna, which incorporates 16 stainless steel ribs with C-shaped cross-sections and a metallic mesh reflector. A custom folding mechanism was designed to facilitate quasi-static wrapping by inducing controlled rotation of the central hub. Torque sensors were integrated to measure the folding moments, and high-speed, high-resolution cameras were employed to capture the dynamic deployment process. Subsequently, finite element (FE) models were developed to simulate the deformation of the antenna during folding and deployment, and the results were validated against experimental data. In addition, the design and analysis of a larger 4.0-meter-aperture wrapped-rib antenna was proposed, utilizing 16 composite thin-walled lenticular tube (CTLT) booms as flexible ribs. This extended study aims to evaluate the scalability and performance of wrapped-rib architectures for future space applications.

The remainder of this paper is structured as follows: Section 2 presents the experimental methods, including the design and fabrication of the antenna, as well as the experimental testing setup. Section 3 outlines the simulation models used to analyze folding and deployment. Sections 4 and 5 present the results for the 0.6-meter and 4.0-meter antennas, respectively, followed by a discussion of the findings in Section 6.

2. Experiments

2.1. Fabrication

Fig. 2 shows the design of the 0.6-meter aperture wrapped-rib antenna used in the experiments. The antenna has a 600 mm aperture diameter and a focal length of 165 mm. The central hub consists of two layers: the inner hub is cylindrical with a diameter of 64.2 mm and features C-shaped slots to secure the ribs, while the outer hub is conical with a diameter of 70 mm and a tilt angle of 84.8°. This design facilitates the wrapping of the ribs. Sixteen ribs are inserted into the slots of the inner hub and fastened in place. Each rib is installed at an angle of 45° between its projection line and the tangent line of the hub at the point of attachment. The metallic mesh reflector is then tensioned and secured to the ribs.

The ribs were fabricated from a custom thin-walled steel alloy, whose chemical composition is listed in Table 1. The material's mechanical properties were characterized through uniaxial tensile tests performed on an Instron testing machine in accordance with the GB/T

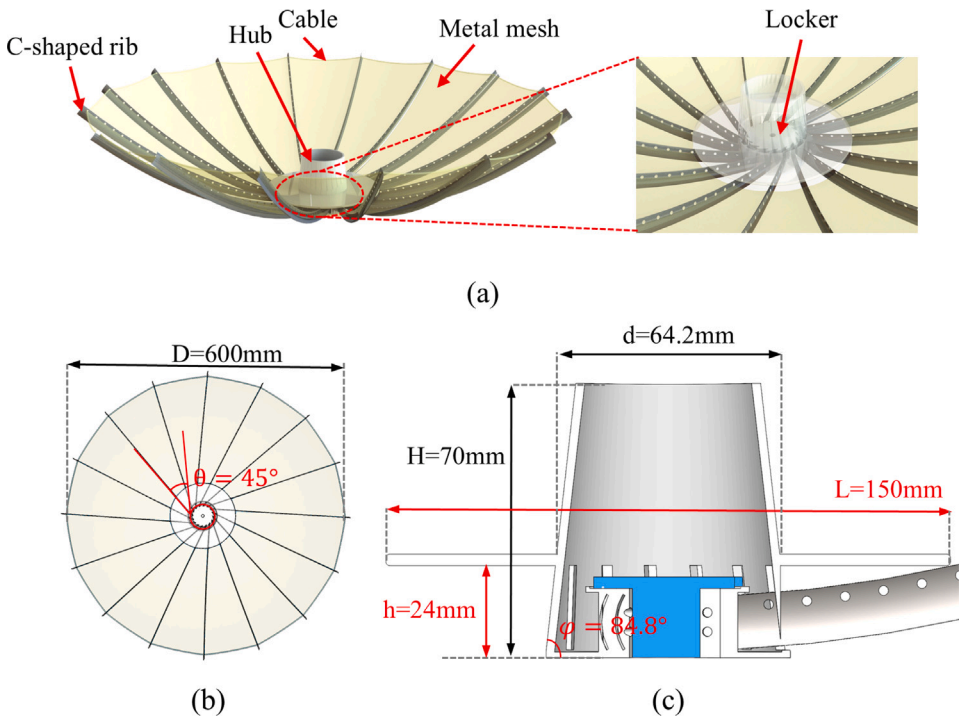

Fig. 2. Design of the wrapped-rib antenna. (a) The antenna consists of 16 ribs that support the metallic mesh, with a central hub at the core. (b) A top view showing the geometric parameters of the antenna. (c) The design and geometry of the central hub.

228.1–2021 standard. The results revealed typical elasto-plastic behavior, with a linear elastic modulus of approximately 80 GPa and a yield strength of 1.495 GPa. The geometry and principal dimensions of the rib are presented in Fig. 3a. The upper edge of each rib follows a parabolic profile, defined by the antenna's aperture diameter and focal length. The cross-section of the rib is C-shaped, formed by a circular arc with a radius of 15 mm and an extended angle of 56°. The ribs were manufactured using a stamping process, and the final products are shown in Fig. 3b. A series of 2.5 mm diameter holes were drilled along the upper edge of each rib to facilitate fastening of the metallic mesh reflector. Wu et al. [18] proposed a forming method involving form-finding first, then fabricating a cutting template based on the form-found mesh, applying prestress by hanging weights around the edges, and finally cutting the mesh under tension. This study adopts the following forming method. First, a form-finding analysis is performed to ensure that the surface accuracy satisfies the required tolerance [38]. The stress within each three-dimensional surface segment spanning between adjacent ribs is then released, and the resulting stress-free geometry is projected onto a flat plane, see Fig. 3c. On this planar pattern, boundary lines are drawn to indicate the precise locations where the mesh will be stitched to the rib holes using thin Kevlar cords. When the mesh pieces — cut and sewn according to this stress-free planar projection — are mounted onto the ribs and the structure is restored to its curved three-dimensional configuration, the mesh naturally develops a pre-tensioned state and satisfies the required surface accuracy. The completed antenna prototype is shown in Fig. 3d. The central hub was fabricated using Weilai R4600 resin and produced with a stereolithography (SLA) 3D printer.

2.2. Experimental testing setup

To facilitate the folding and deployment behavior testing of the wrapped-rib antenna, a custom folding mechanism was designed, as has been illustrated in Fig. 1. The mechanical design of the wrapped-rib antenna and its folding and deployment mechanisms are shown in Video S1 in the Supporting Materials. The mechanism consists of sixteen vertical columns fixed to a circular base plate, matching the radial arrangement of the wrapped ribs. The antenna is inserted into the mechanism along a central shaft, and the entire assembly is secured to an experimental table. To automate the folding process and measure the associated folding moments, a dedicated experimental setup was developed, as schematically shown in Fig. 4a. Rotational actuation is provided by a motor, and a torque sensor connected to a computer records the torque data in real time. The motor's rotation is transmitted through a 90-degree steering mechanism to the drive shaft, which rotates the central hub of the antenna. This rotation causes the ribs and reflector to fold and wrap into the space between the central hub and the surrounding folding mechanism. During the test, the motor maintains a constant rotation rate of 2.5 revolutions per minute, enabling quasi-static folding while the folding moment is continuously recorded. Once folding is complete, a cylindrical cover is placed over the folded antenna and folding mechanism from above. The folding mechanism is then removed from below, leaving the antenna fully folded and stowed, secured within the cylindrical cover. For deployment testing, the cover is rapidly removed from the top, allowing the antenna to deploy by releasing the strain energy stored in the deformed ribs. The reflector, attached to the ribs, simultaneously unfolds and is supported in the deployed configuration. Two high-speed, high-resolution cameras are used to capture deployment snapshots from both top and front views. The complete experimental setup and associated equipment are shown

Table 1
Chemical composition of C-shaped ribs.

Item	C	Mn	P	S	Si	Cr	Ni
Composition (%)	0.091	1.19	0.019	0.021	0.61	16.86	7.12

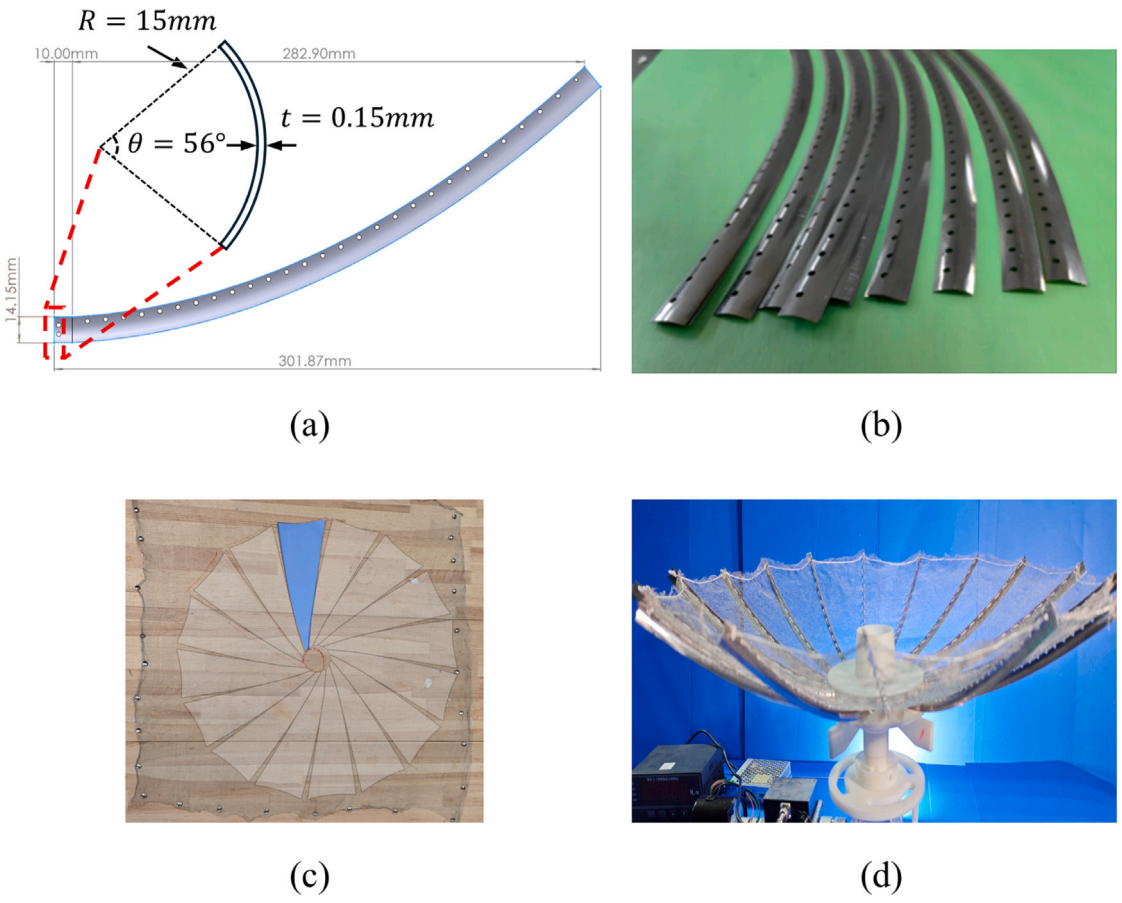

Fig. 3. Design and fabrication of the rib and metallic mesh reflector. (a) Geometric design and parameters of the rib. (b) Rib products. (c) Metallic mesh membrane labeled with (d) The assembled wrapped-rib antenna.

in Fig. 4b. For each test conducted on the experimental setup, three repeated trials were performed to reduce the influence of random variations.

3. Simulations

The simulation model was developed using the commercial finite element software ABAQUS 2020. Fig. 5a illustrates the simulation model along with its finite element mesh representation. To efficiently simulate the folding and deployment behavior, the wrapped-rib antenna model includes all 16 ribs and the reflector. The ribs and reflector are both modeled using isotropic, linear elastic material behavior. The ribs have a Young's modulus of 80 GPa and a Poisson's ratio of 0.3. The membrane material properties are defined with a Young's modulus of 1.7 MPa and a Poisson's ratio of 0.27 [43]. The membrane was subjected to a prestress of 0.07 MPa by means of cooling. The ribs are discretized using thin shell elements (ABAQUS element type: S4R), while the reflector is modeled with membrane elements (ABAQUS element type: M3D4R). A mesh independence study was conducted to verify that the numerical results were not sensitive to mesh resolution. Based on this study, the adopted discretization was selected as a compromise between accuracy and computational efficiency, resulting in approximately 1092 shell elements for each rib and 79872 membrane elements for the reflector. *Tie constraints are applied at the connected boundaries to simulate the fastening between the ribs and the reflector. The central hub and folding mechanisms are modeled as rigid bodies and discretized using R3D4 elements in ABAQUS. As shown in Fig. 5b, the ribs are inserted between the gaps of adjacent columns of the folding mechanisms, and the end sections of the ribs are connected to the reference point at the center of the central hub using an *MPC constraint. This configuration effectively simulates the attachment of the ribs to the central hub. A contact property was defined between the ribs and the folding mechanisms using an Abaqus contact pair. The normal contact behavior was modeled as hard contact, while the tangential behavior was governed by a friction coefficient of 0.3. Contact interactions involving the membrane were simplified to include only normal contact behavior, modeled as hard contact, with frictionless tangential behavior. This simplification was adopted to enhance numerical robustness, as preliminary simulations showed that introducing membrane friction led to significantly increased computational cost and severe convergence difficulties. Although membrane friction may influence the deployment behavior observed experimentally, its effects were neglected in the present model to ensure stable and efficient numerical simulations. The simulations were performed using the Abaqus/Explicit dynamic solver. Geometric nonlinearity was fully accounted for by enabling the `NLGEOM` (large-displacement) option, thereby capturing the large rotations, large deflections, and configuration-dependent stiffness that occur during both the folding (wrapping) and deployment processes. For the folding behavior, a rotational displacement was applied to the reference point of the central hub, causing the flexible ribs to fold through contact with the folding mechanisms, as observed in the experiments. To effectively simulate the folding and deployment behavior and overcome convergence issues, the explicit dynamic solver was employed [44]. Mass scaling was applied using the target time

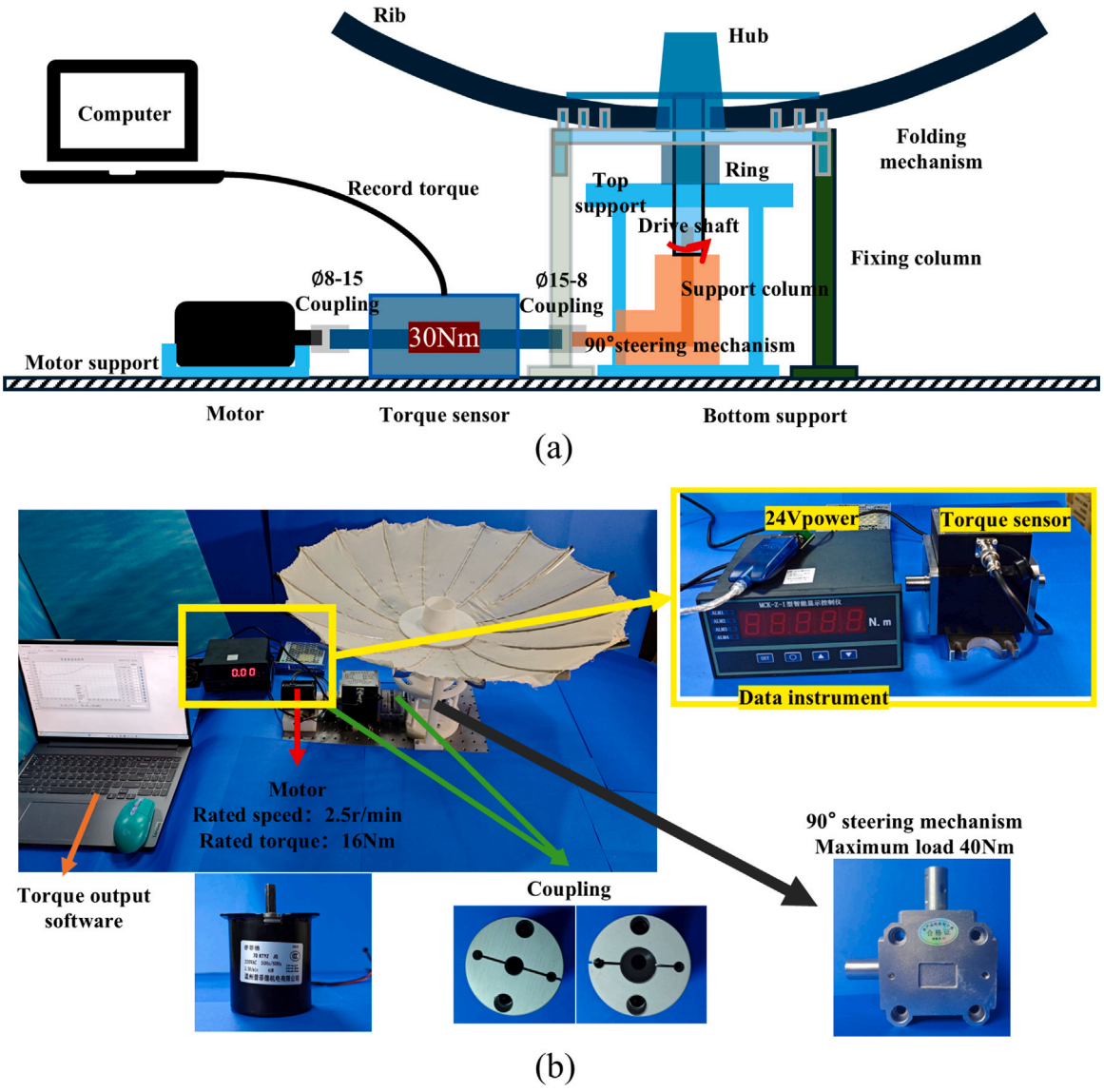

Fig. 4. Experimental set-up. (a) Schematic diagram. (b) Actual setup with equipment.

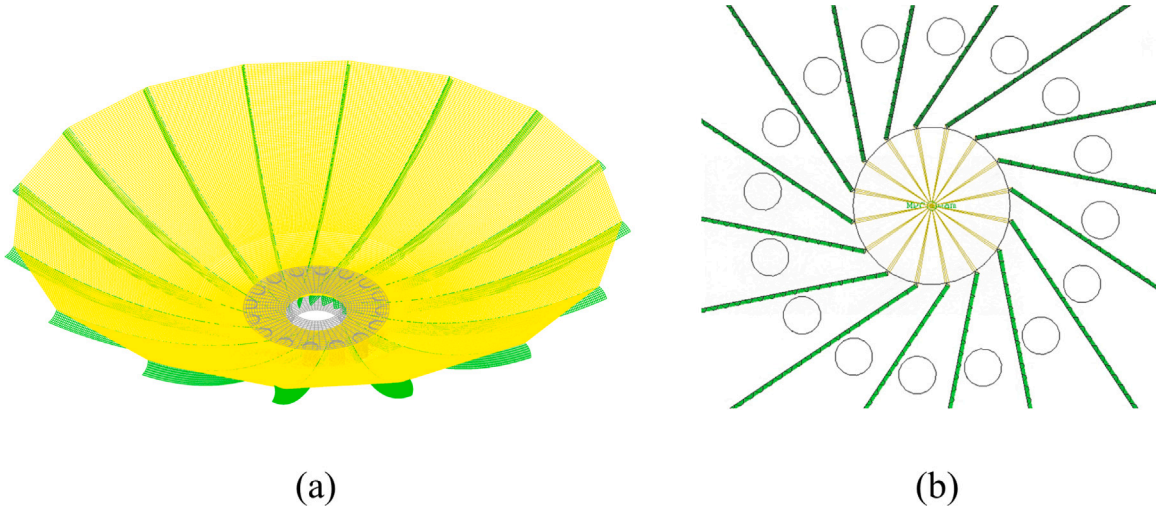

Fig. 5. FE model of the wrapped-rib antenna. (a) Side view. (b) Top view.

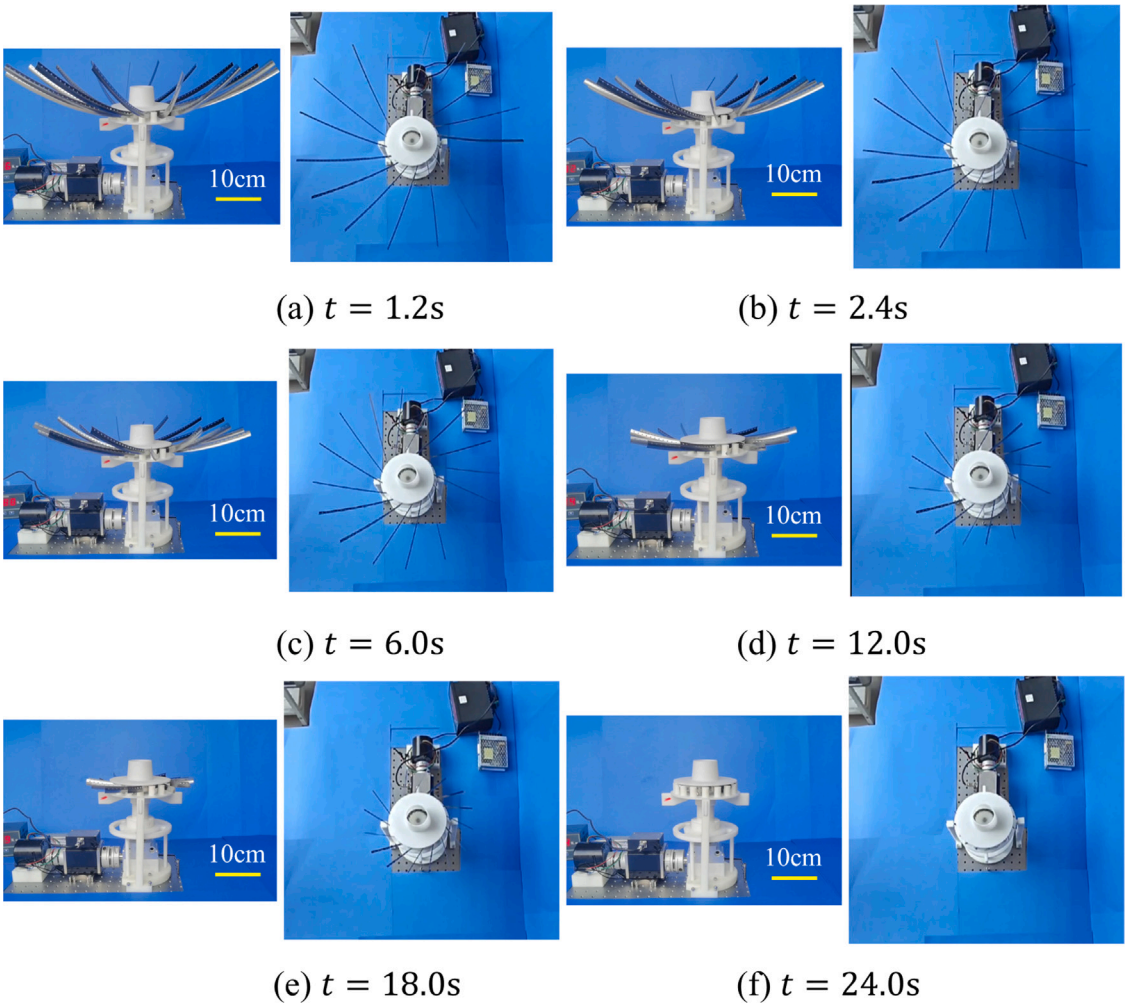

Fig. 6. Experimental snapshots showing the folding behavior of the parabolic ribs during the wrapping process.

increment option, with the target time increment set to 1×10^{-6} s. The folding process was simulated under a quasi-static condition by monitoring the kinetic energy as a small amount of the strain energy. On the other hand, the deployment was modeled as a transient dynamic process, actuated by releasing all contact interactions between the flexible ribs and the folding mechanisms in the simulation, while constraining the rotation of the central hub during deployment. It is important to note that during both folding and deployment, the membrane reflector adjusts its position to align with the deformation of the ribs.

4. Results of the 0.6-meter antenna

4.1. Folding behavior

4.1.1. Folding of wrapped-ribs

With the experimental setup and simulation model described above, we begin by investigating the folding behavior of the flexible ribs without considering the reflector. Fig. 6 shows the experimentally observed wrapping process of the parabolic ribs. As the central hub rotates, all of the ribs are folded and wrapped around the central hub. The process is driven solely by the motor, and the folding moments are recorded over time. Since the central hub rotates very slowly, the folding process is quasi-static.

In the simulation, the results also indicate a similar folding process of the ribs, as shown in Fig. 7. From the FE results, it can be seen that the maximum von Mises stress in the ribs increases as the folding proceeds. However, even at the final fully folded state, the maximum von Mises stress is about 934.7 MPa, which is far less than the yield strength of the raw material for the rib—1.495 GPa. This suggests that no plastic deformation occurs and confirms the accuracy of using a linear elastic material model for the rib. Furthermore, in the experiments, no permanent deformation was observed after hundreds of folding and deployment cycles. The experiments and simulations of the folding and deployment behavior of the flexible ribs are provided in Video S2 in the Supporting Materials. The folding moment is plotted as a function of rotation time in Fig. 8a for experiments and in Fig. 8b for simulations. In addition to the folding behavior of all 16 ribs, we also investigated the folding behavior of 2, 4, and 8 ribs for comparison. The results show that as the folding progresses, the folding moment increases rapidly initially, reaches a peak value, then drops sharply, and finally stabilizes to a steady folding moment. The peak moment corresponds to the buckling and localized folding of the ribs, similar to the behavior observed in tape-spring folding [45]. It is found that as the number of ribs increases, the peak moment also increases proportionally. The experimental and simulation results exhibit the same general trend, and the peak moments are in good agreement. However, a discrepancy is observed in the steady folding moment during the

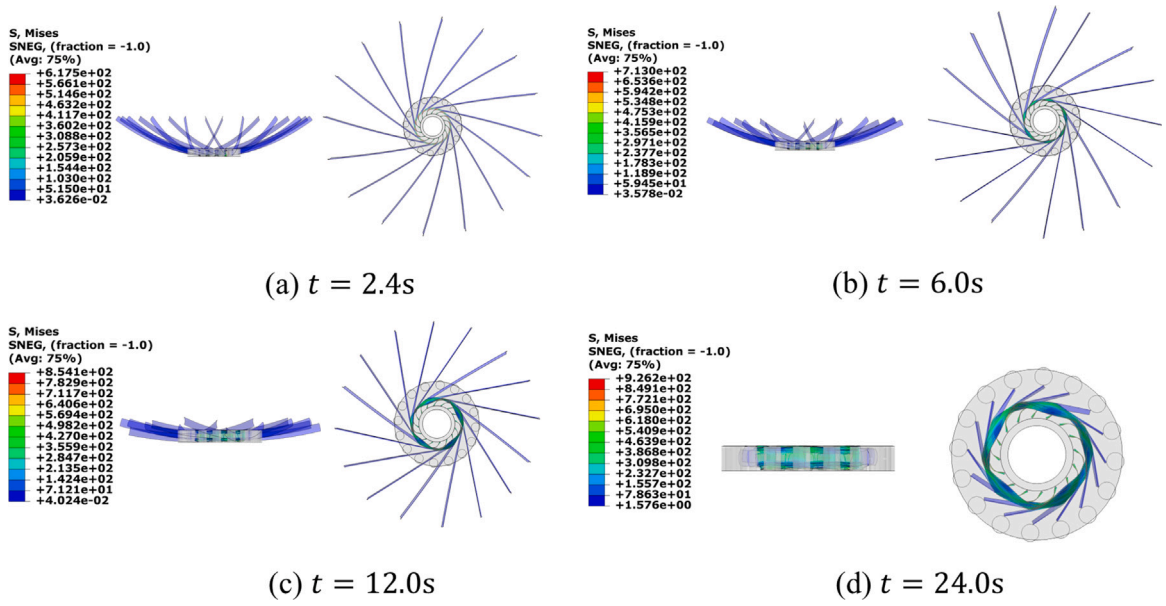

Fig. 7. FE simulation snapshots displaying the von Mises stress distribution during the folding behavior of the parabolic ribs.

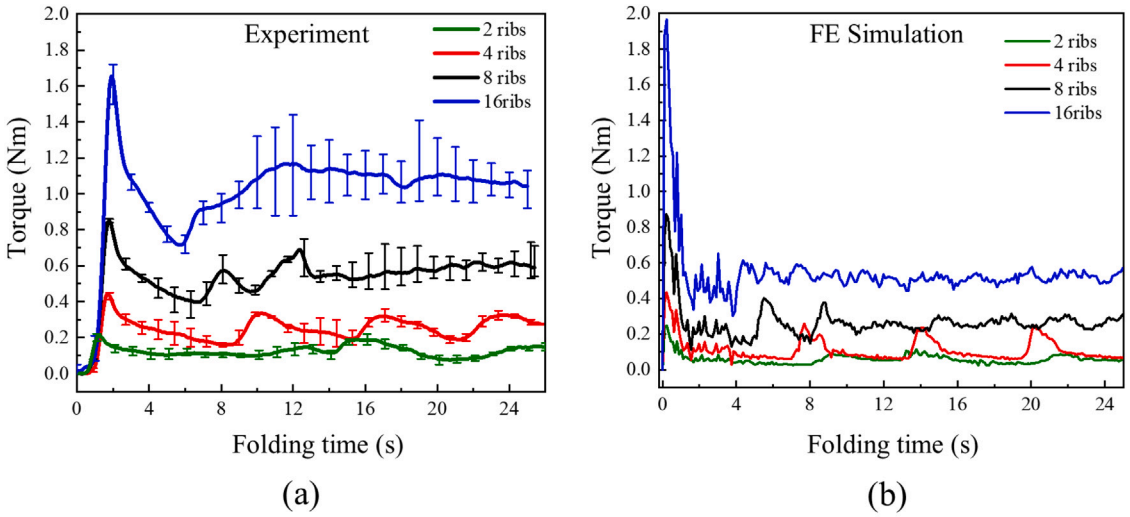

Fig. 8. Folding moment as a function of rotation. (a) Experimental results. (b) Simulation results.

latter stage of the folding process, where the experimental value is much higher than that of the simulation. This difference is attributed to the complex contact and friction observed in the experiments, as the edges of the ribs interact with the folding mechanisms. While a contact property was defined in the simulations, accurately simulating the contact forces between the edges of the ribs and the surface of the mechanisms remains challenging. Fig. 9 shows comparisons of the fully folded state of 2, 4, 8, and 16 parabolic ribs in both experiments and simulations. It can be observed that the folded state of the ribs is non-uniform due to the relatively large stowage space. As the number of ribs increases, the folds become less localized, gradually approximating a circular deformation. These results are consistent with the analysis of non-uniform folding behavior in tape-springs recently presented by Yan et al. [34].

4.1.2. *Folding of wrapped-rib antenna*

Next, we investigate the folding behavior of the wrapped-rib antenna, in which the reflectors deform in coordination with the flexible ribs. Due to the complex interactions among the ribs, the reflector, and the folding mechanism — as well as the ultra-thin steel wires used in the metallic mesh — there is a high risk of local fracture during the folding process [46]. As a result, the folding of the antenna equipped with a metallic mesh reflector cannot be fully automated using the current experimental setup. To facilitate measurement of the folding moment, we fabricated a test version of the antenna using a stretchable gauze mesh fabric made of polyester and spandex as the reflector. The folding process of this modified antenna is shown in Fig. 10, while Fig. 11 presents the corresponding folding process obtained from simulation.

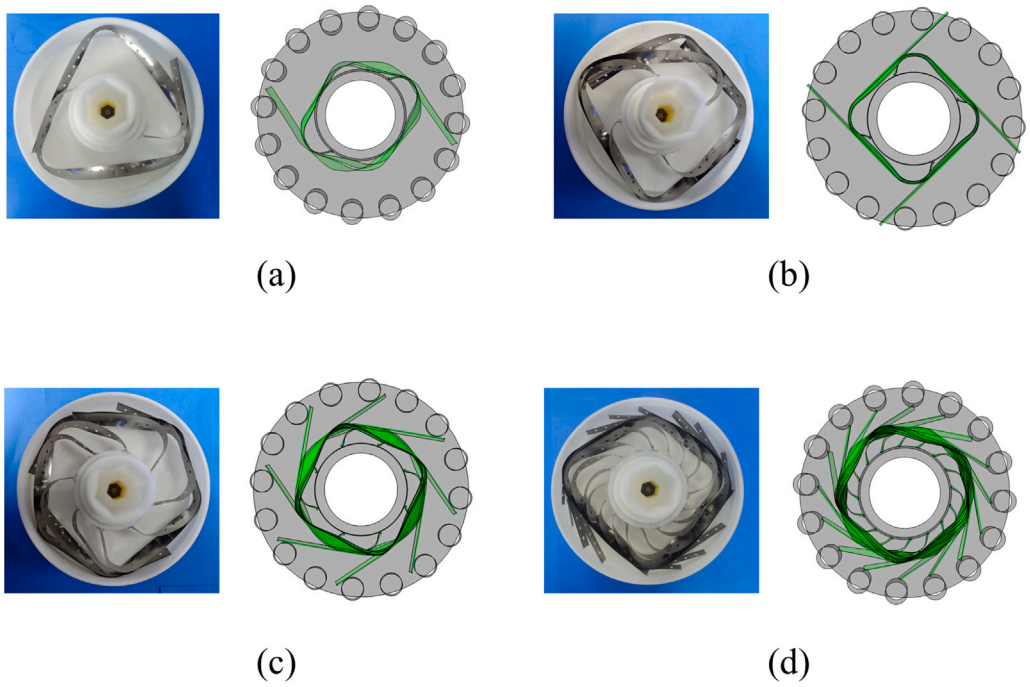

Fig. 9. Comparison between experiments and simulations of the fully folded state of the parabolic ribs. (a) Two ribs. (b) Four ribs. (c) Eight ribs. (d) Sixteen ribs.

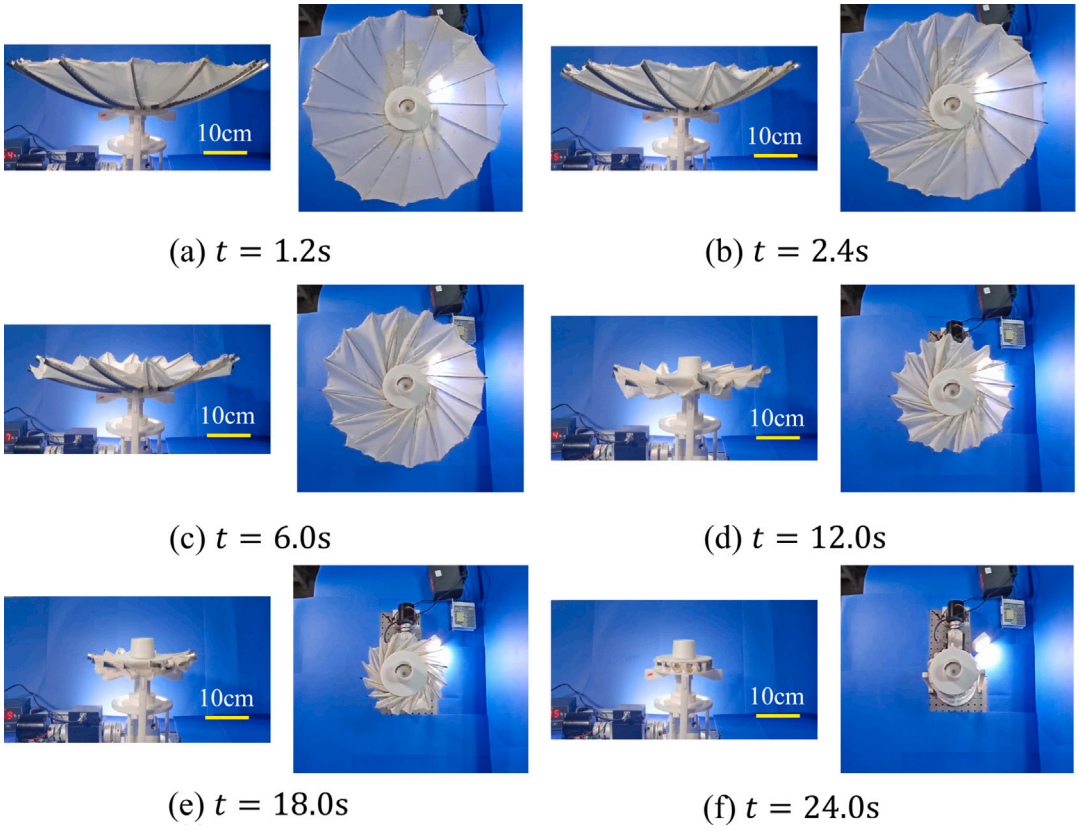

Fig. 10. Experimental snapshots showing the behavior of the ribs and reflector during the folding process of the antenna.

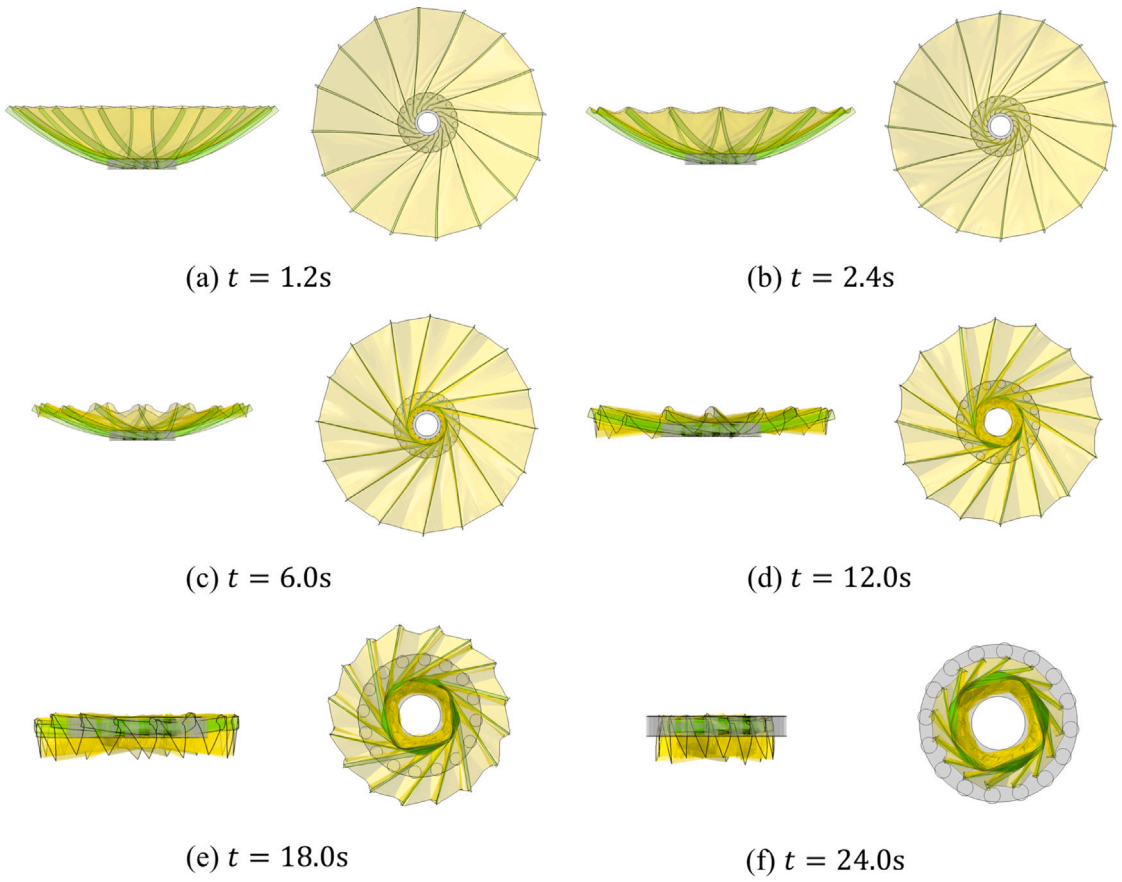

Fig. 11. FE simulation snapshots showing the behavior of the ribs and reflector during the folding process of the antenna.

The measured wrapping torque during folding is plotted in Fig. 12a. A similar trend to that in Fig. 8a is observed during the initial folding stage: the torque rises rapidly, reaches a peak, and then drops. However, in the subsequent steady folding phase, the torque significantly increases instead of forming a plateau as seen in Fig. 8a. This difference arises from the continued contact and interaction between the membrane, the ribs, and the folding mechanism as the components are packed together. The antenna with the metallic mesh reflector was folded manually, with the mesh carefully arranged between adjacent ribs to prevent damage. As the central hub rotates, the antenna folds and wraps into a compact volume, resulting in a significantly reduced height compared to the deployed configuration. The antenna's dimensions are reduced in both aperture diameter and height. The final stowed configuration has a diameter of 160 mm and a height of 24 mm, determined by the size of the folding mechanism. Figs. 12b, 12c, and 12d show the stowed configurations of the antenna with the stretchable mesh fabric, the metallic mesh reflector, and the simulation results, respectively. Figs. 12b shows that, because the ribs fold into a regular pattern, the mesh fabric becomes neatly sandwiched between adjacent ribs and sags under its own weight in the stowed state. Upon deployment, the rib-supported mesh unfolds in an orderly manner, with no interference or tearing observed between mesh panels. By contrast, the metallic mesh in Figs. 12c is susceptible to damage from the ribs' sharp edges during folding. To avoid this, we folded the metallic mesh by hand: as the ribs were rotated to close, the mesh was smoothed and arranged so its surface remained as flat as possible. This manual packing produced a similarly regular stowed geometry and helped ensure reliable, damage-free deployment. It should be noted that the experimental prototype inevitably includes manufacturing tolerances and mechanical clearances arising from fabrication and assembly. In particular, a certain level of hinge backlash exists in the folding mechanism, and frictional effects are present at hinges, contact interfaces, and within the folding system. These factors contribute to energy dissipation during the folding process and are reflected in the gradual increase of the measured folding torque observed in the experiments. Due to practical limitations, only a single prototype was fabricated and tested; therefore, the influence of manufacturing tolerances could not be statistically quantified. Nevertheless, the experimental results consistently capture the overall folding behavior and provide reliable insight into the mechanical characteristics of the wrapped-rib antenna. In addition, the discrepancy between the experimental and numerical folding torque responses can be attributed to the idealized assumptions adopted in the FE model. The numerical simulations assume a perfectly symmetric configuration without hinge clearance or membrane friction, causing the ribs to deform and buckle nearly simultaneously and resulting in a slightly higher peak folding torque. In contrast, experimental installation tolerances lead to non-uniform folding among individual ribs, which distributes the deformation process and reduces the measured peak torque.

4.2. Deployment behavior

4.2.1. Deployment of wrapped-ribs

Figs. 13 and 14 present snapshots of the dynamic deployment process of the wrapped ribs without the membrane reflector, captured from experiments and FE simulations, respectively. Upon removal of the constraints, the folded ribs are released by the stored strain energy and begin to deploy. The ribs unfold in a non-synchronized, random

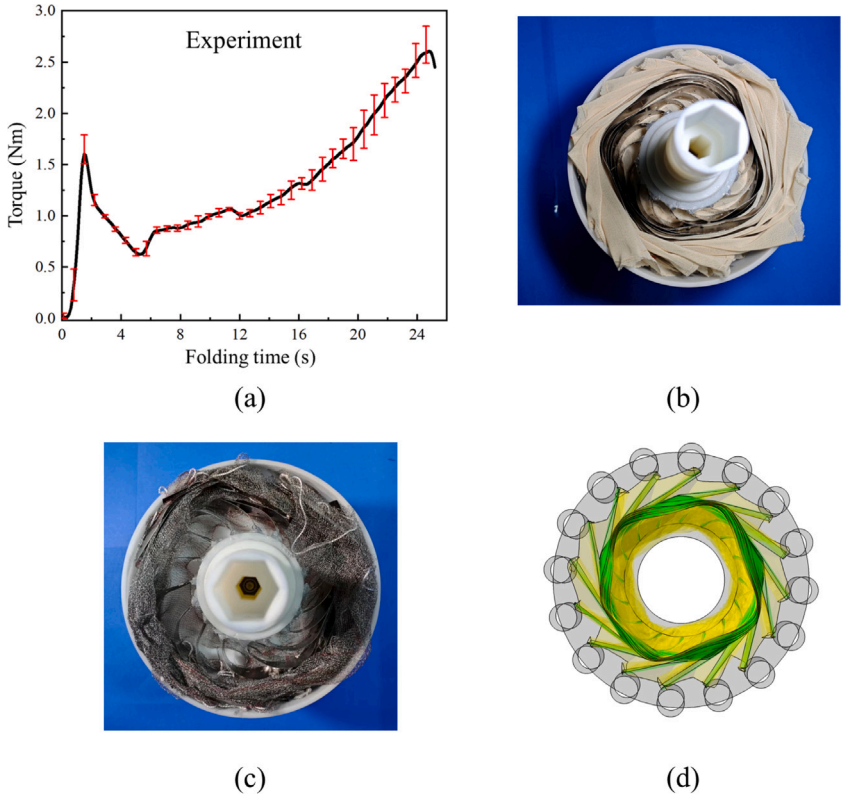

Fig. 12. Folding and stowed state of the wrapped-rib antenna. (a) Torque versus folding time for the stretchable fabric reflector. (b) Stowed state of the wrapped-rib antenna with a stretchable gauze mesh fabric as reflector. (c) Stowed state of the wrapped-rib antenna with a metallic mesh as reflector. (d) Stowed state of the FE simulation result.

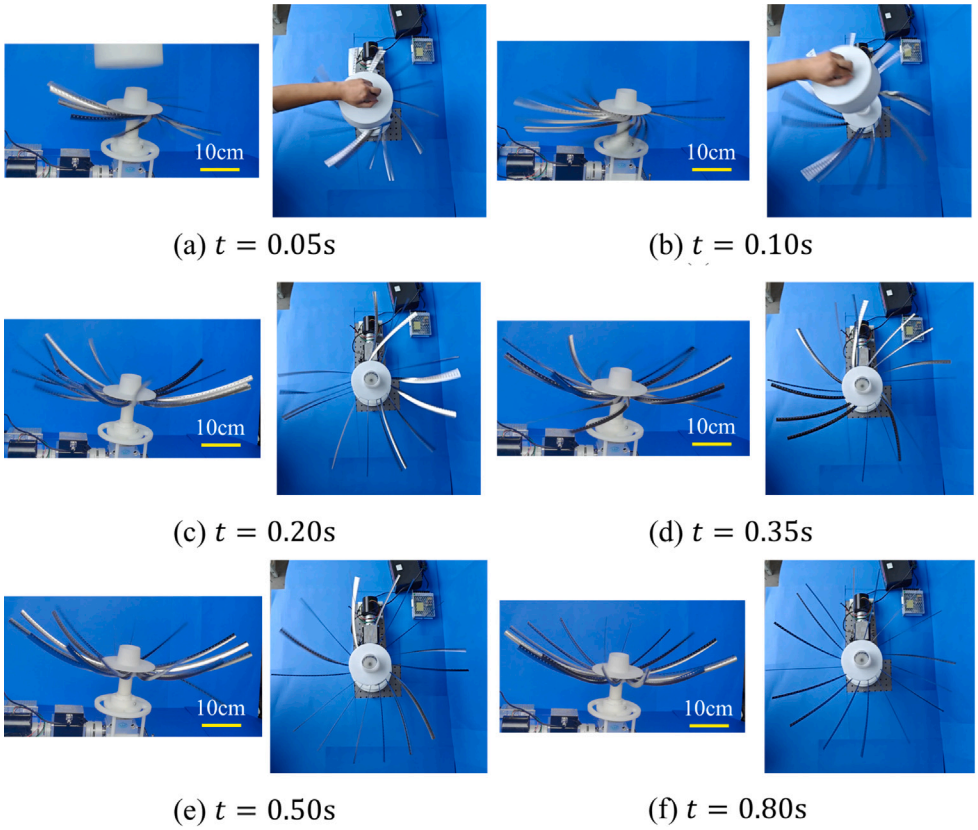

Fig. 13. Experimental snapshots showing the dynamic deployment process of wrapped-ribs without the reflector.

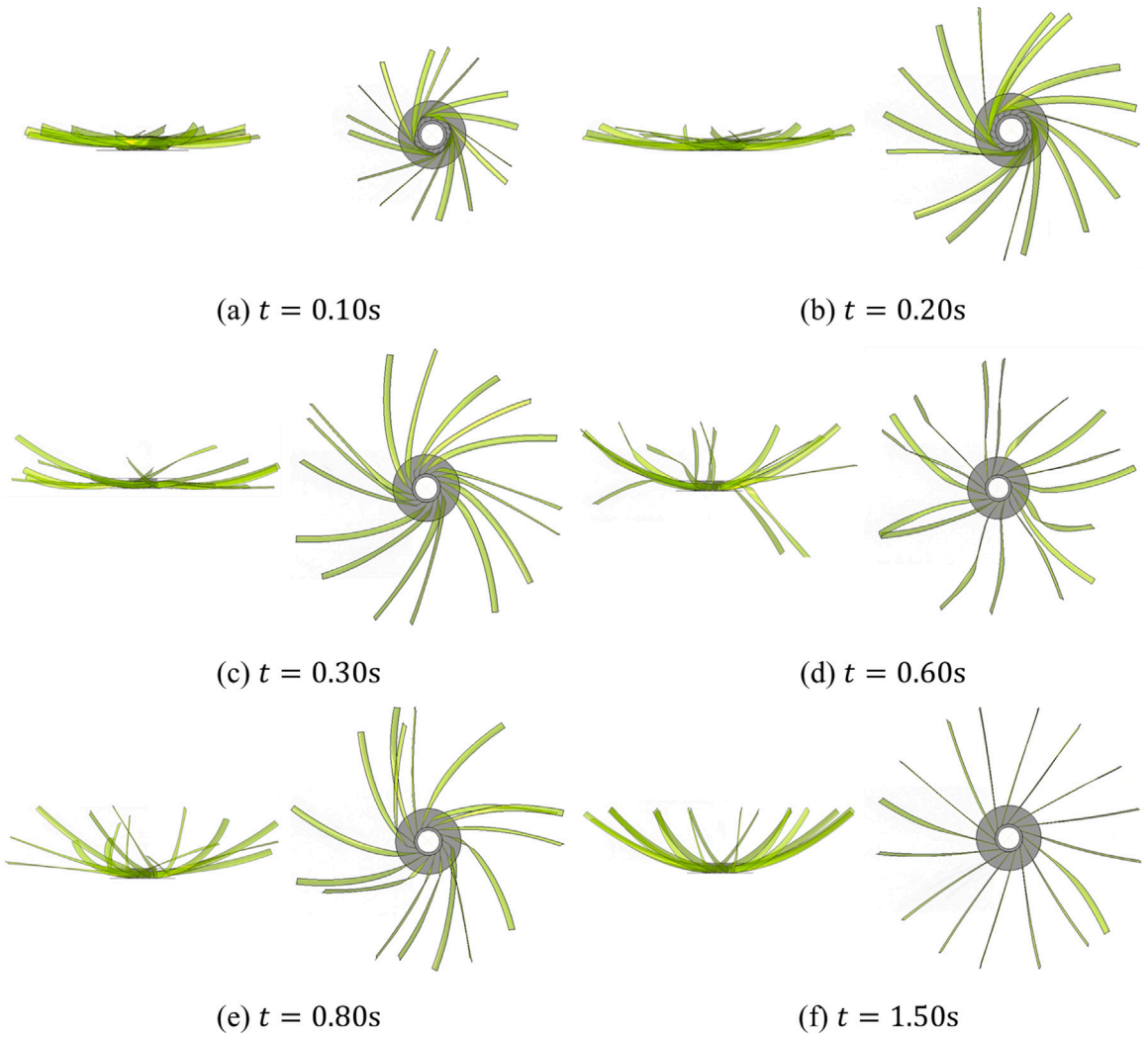

Fig. 14. FE simulation snapshots showing the dynamic deployment process of wrapped-ribs without the reflector.

manner. Within approximately 0.8 s, all ribs return to their original shapes with negligible plastic deformation, indicating a fully elastic folding and deployment behavior. It is worth noting that, because the experiments were conducted in air, the deployment time — defined as the duration from the removal of the cover to the cessation of rib vibrations — differs slightly between the experimental and simulated results. Moreover, in the experiments, deployment was initiated by manually removing the stowage cover. Due to manufacturing and assembly tolerances, the ribs do not share identical stowed configurations, and the manual release process cannot be perfectly synchronized. These factors lead to more irregular and less repeatable deployment trajectories compared to the numerical simulations, which assume identical initial states and simultaneous release of all ribs. To account for air damping in the simulation, a small amount of viscous pressure was applied to suppress post-deployment oscillations. Consequently, the simulated deployment time is sensitive to the magnitude of the applied viscous damping.

4.2.2. Deployment of wrapped-ribs with the membrane reflector

In contrast, during the deployment of the wrapped-rib antenna, the presence of the membrane causes the ribs to deploy in a synchronized manner. Figs. 15 and 16 show experimentally captured snapshots of the deployment process for antennas equipped with the elastic fabric and the metallic mesh reflector, respectively. The progression of membrane tension is clearly visible, transitioning from a wrinkled, stress-free state to a fully tensioned, stressed state. It is worth noting that the metallic mesh reflector possesses a higher effective modulus than the elastic fabric, and as a result, the antenna with the metallic mesh deploys more rapidly than the one with the elastic fabric. To assess the repeatability and structural integrity of the deployment process, all experiments were repeated at least three times under identical conditions, using the same set of metallic ribs without replacement. In all repeated tests, the wrapped ribs successfully deployed without jamming or failure, and no visible damage or permanent deformation of the ribs was observed after deployment. These observations indicate that the deployment process is reliable and that the structural integrity of the antenna is well maintained throughout repeated folding and deployment cycles. Quantitative evaluation of post-deployment surface accuracy or stiffness could serve as more rigorous performance indicators; however, such measurements are beyond the scope of the present experimental setup and are left for future investigations.

Next, Fig. 17 presents snapshots from FE simulations of the dynamic deployment process of the wrapped-rib antenna. As shown in the simulation results, the membrane elements in ABAQUS are effective in capturing both the wrinkling and the tensioning behavior of

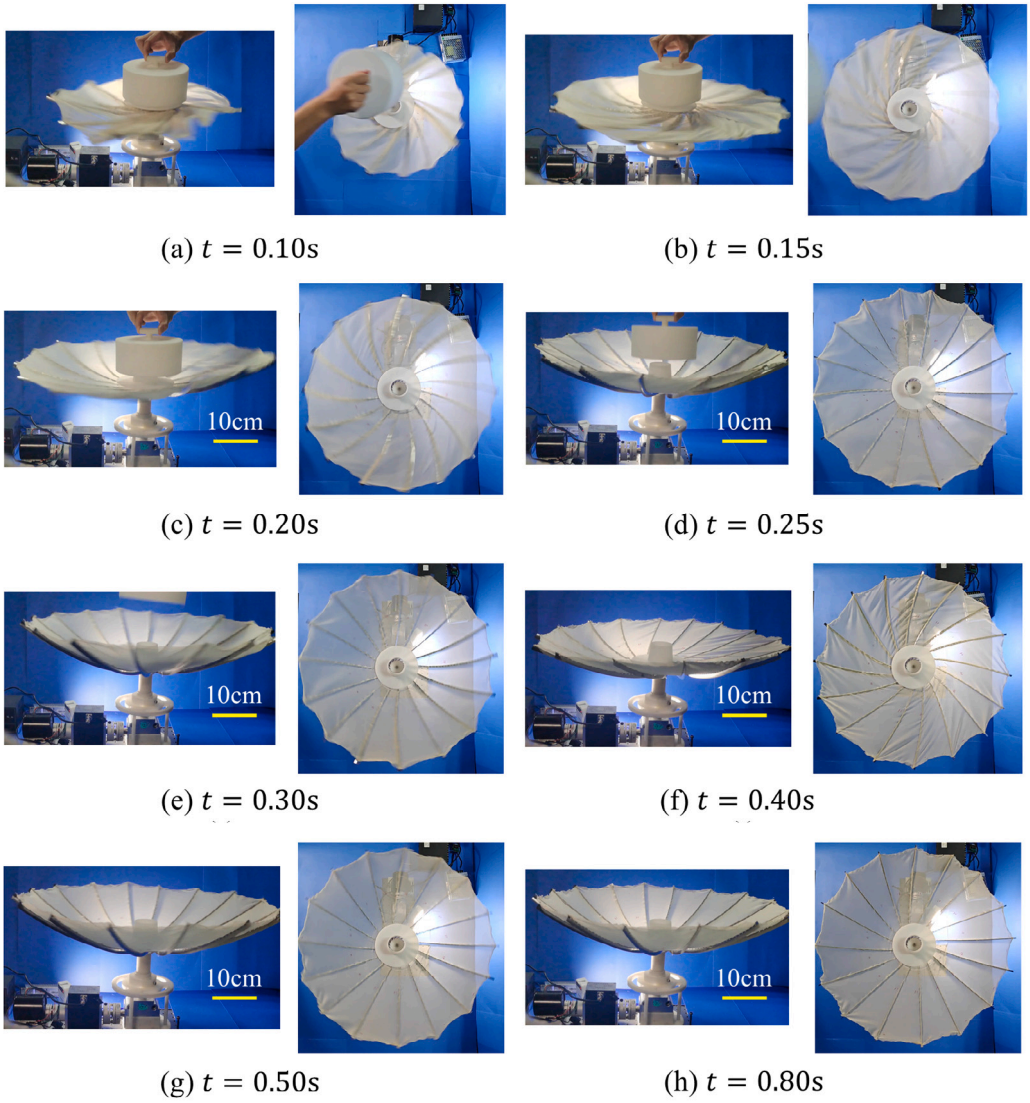

Fig. 15. Experimental deployment snapshots of the wrapped-rib antenna with an elastic fabric reflector.

the reflector. To quantitatively evaluate the packaging efficiency and dimensional changes during the folding and deployment process, we define a virtual cylinder that envelopes the antenna at any intermediate configuration, characterized by a radius R and a height H. In the fully deployed state, the corresponding dimensions are R_0 and H_0. The normalized packaging metrics are then defined as

$$R^* = \frac{R_0 - R}{R_0}, \qquad H^* = \frac{H_0 - H}{H_0},$$

which represent the relative reduction in radius and height, respectively.

Figs. 18a and 18b show the evolution of R^* and H^* throughout the folding and deployment processes. During folding, R^* decreases steadily from 1 to approximately 0.202, while H^* decreases from 1 to 0.117. The reduction in R^* is nearly linear, whereas H^* decreases rapidly at first and then more gradually. In contrast, during deployment, R^* increases more rapidly than H^* in the initial stage, indicating that the antenna first expands radially before extending vertically. The folding and deployment behavior of the 0.6-meter-aperture wrapped-rib antenna is provided in Video S3 in the Supporting Materials. In addition, the FE simulations provide further insights into the mechanical behavior. Fig. 18c shows the torque required for folding, as well as the reactive torque exerted by the antenna on the fixed constraint for deployment. Fig. 18d illustrates the evolution of strain energy: energy is gradually stored during folding and then rapidly released over a short duration during deployment.

4.3. Parametric study: effect of reflector prestress and gravity effects

In this section, we use the numerical model to quantify the influence of initial conditions, including membrane prestress and gravity, on the folding and deployment processes. Starting from a baseline mesh prestress of 0.07 MPa, two additional tension levels (0 MPa and 0.14 MPa) were considered. The influence of mesh tension on the folding sequence was first evaluated. Fig. 19a and c plot the antenna radius, height, and stowage torque as functions of folding time. These results indicate that mesh tension has only a minor effect on the folding morphology and on the overall folding torque after rib buckling. This insensitivity is attributed to rapid relaxation of the mesh once folding begins, so the mesh exerts little sustained constraint during folding.

Fig. 16. Experimental deployment snapshots of the wrapped-rib antenna with a metallic mesh reflector.

However, a clear trend is observed in the peak torque: higher mesh tension corresponds to a lower peak torque. This effect can be explained by the fact that, under larger prestress, the mesh draws the ribs more strongly toward the center in the deployed configuration, reducing the overlap area when ribs wrap around the central hub; with zero mesh tension, ribs tend to overlap nearly completely during wrapping, which produces a larger simultaneous-buckling peak torque. The deployment behavior is shown in Fig. 19b and d. Larger mesh tension promotes more rapid decay of post-deployment oscillations in both geometry and torque, indicating that mesh tension suppresses the ribs' rebound during deployment.

It should be noted that the experimental tests presented in this work were conducted under normal gravity and atmospheric conditions due to practical constraints associated with ground-based testing. As a result, the experimental setup cannot fully reproduce the microgravity and vacuum environment encountered in space. Nevertheless, the numerical model enables us to examine the influence of gravity on the folding and deployment processes. Figs. 20a and c show that gravity has only a modest influence on the stowage process, mainly causing a slight reduction in rib height. Figs. 20b and d indicate that gravity accelerates the attenuation of post-deployment oscillations and reduces the resulting recoil torque. Consequently, in a space environment — where gravity and aerodynamic damping are absent — post-deployment oscillations are expected to be more pronounced, and the ribs' recoil torques may impose larger transient dynamic loads on the structure. Importantly, the key performance indicators remain essentially unchanged: the maximum folding torque is nearly identical in the two cases, and both the final folded configuration and the fully deployed state coincide. By contrast, the peak deployment torque is slightly higher in the no-gravity condition, reflecting the more dynamic deployment transient in microgravity.

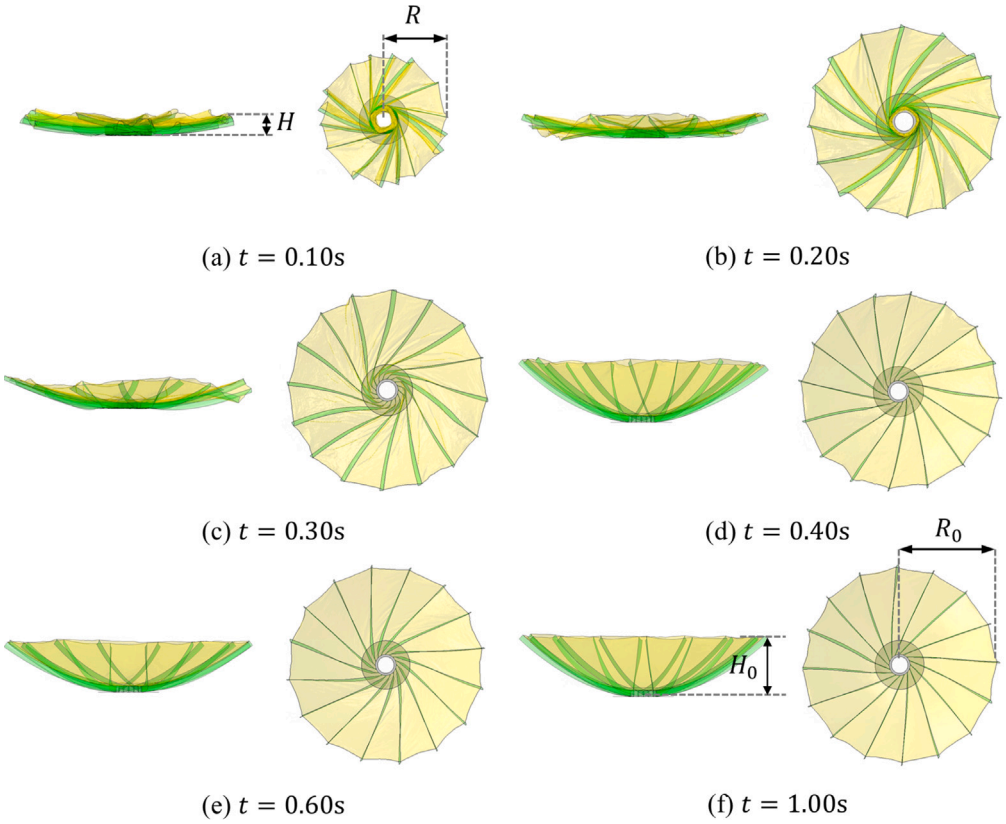

Fig. 17. FE simulation snapshots of the dynamic deployment of the wrapped-rib antenna.

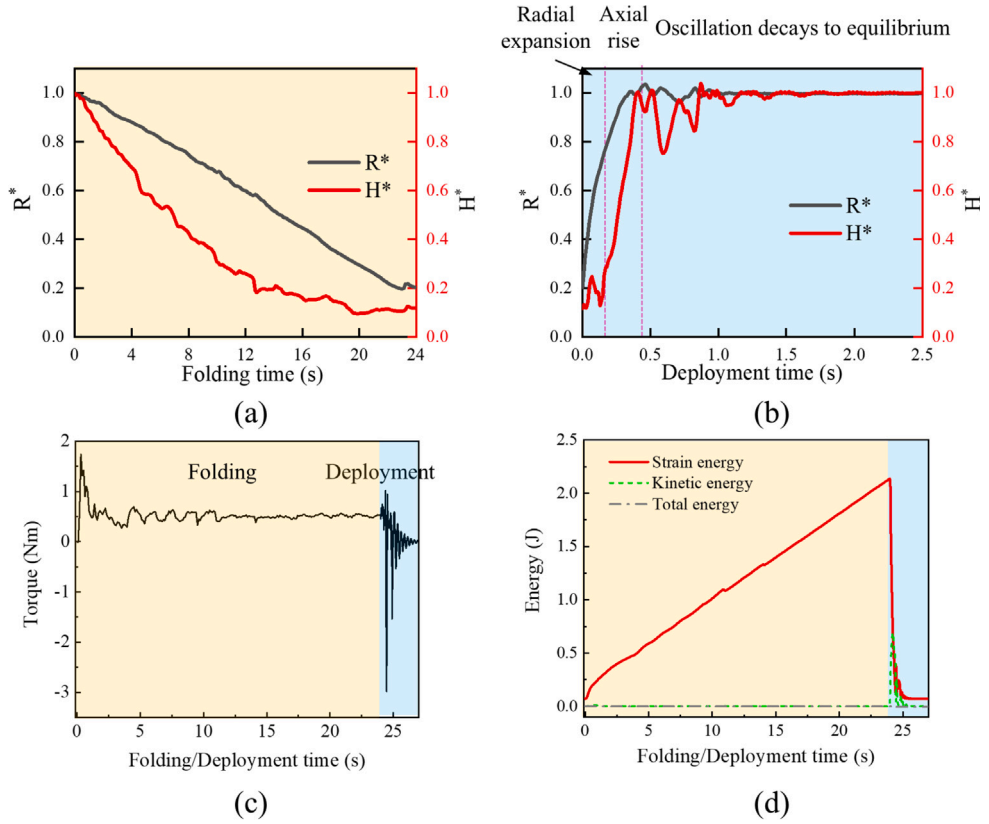

Fig. 18. Folding and deployment behavior of the 0.6-meter-aperture antenna. Normalized height and radius of the antenna throughout the (a) folding and (b) deployment process. (c) Torque and (d) strain energy as a function of the folding and deployment process.

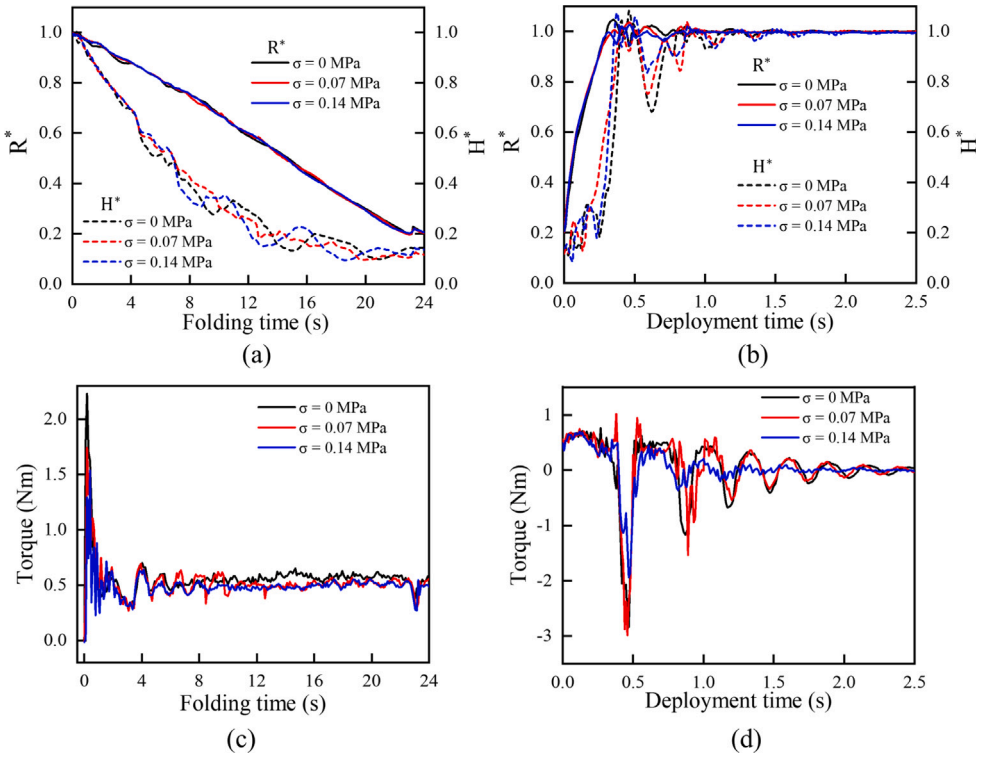

Fig. 19. Effect of mesh prestress on folding and deployment behavior of the 0.6-m aperture antenna. Normalized height and radius of the antenna throughout the (a) folding and (b) deployment process. Torque throughout the (a) folding and (b) deployment process.

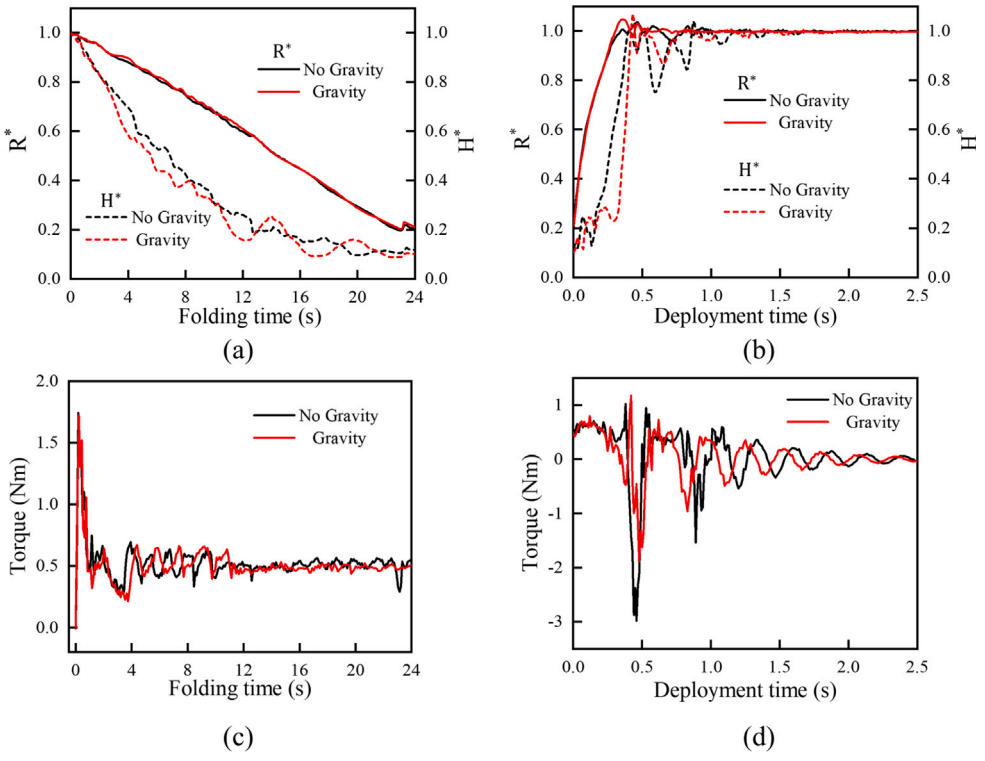

Fig. 20. Effect of gravity on folding and deployment behavior of the 0.6-m aperture antenna. Normalized height and radius of the antenna throughout the (a) folding and (b) deployment process. Torque throughout the (a) folding and (b) deployment process.

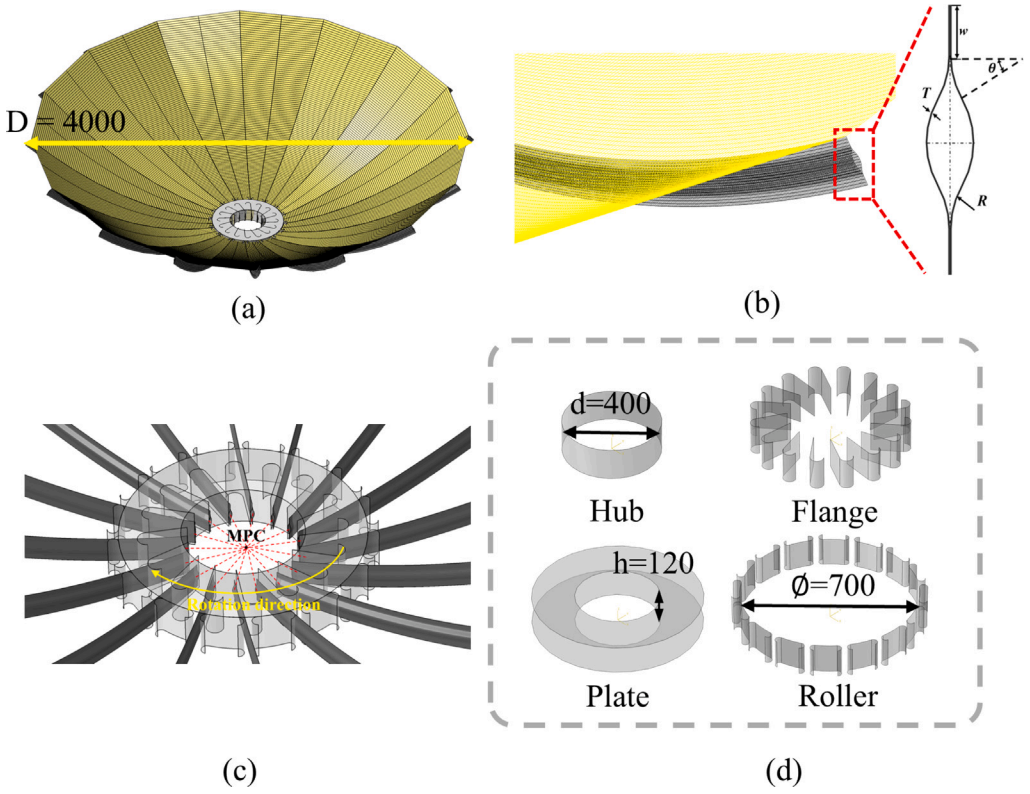

Fig. 21. Design and FE model of the 4-meter-aperture antenna. (a) Overall view of the antenna. (b) Rib made of composite thin-ply laminates with a lenticular cross-section. (c) Central hub and folding mechanism. (d) Components and dimensions of the folding mechanism, including the hub, flanges, plates, and rollers. All dimensions are given in millimeters.

5. Results of the 4.0-meter antenna

5.1. Modeling and simulation setup

Finally, in this section, we extend the design to a larger-aperture antenna with a diameter of 4 meters and a focal length of 1.1 meters; see Fig. 21a for an overall view of the antenna. For this 4-meter-aperture antenna, 16 parabolic ribs made of composite thin-walled lenticular tubes (CTLTs) are employed. The CTLT, also known as the collapsible tube mast (CTM), is a closed tubular structure with a lenticular cross-section, commonly used for deploying large structures in space applications. In our previous studies, we have demonstrated that CTLTs exhibit superior bending resistance compared to triangular rollable and collapsible (TRAC) booms, and that their closed cross-sectional geometry provides enhanced torsional stiffness [47]. The fabrication and deployment performance of CTLTs has also been experimentally and numerically verified in our recent work [32,33]. However, it is worth noting that although CTLTs are widely used in solar sail systems, their application has typically been limited to straight configurations. In contrast, the CTLTs used in this antenna are manufactured with a parabolic curvature, representing a novel and structurally more demanding implementation of this deployable structural concept. As shown in Fig. 21b, the lenticular cross-section of the CTLT is fabricated by joining two Ω-shaped composite shells along a commonly used bonding edge. The cross-section is characterized by the following geometric parameters: width $w = 15$ mm, radius $R = 30$ mm, extended angle $\theta = 25°$, and thickness $T = 0.24$ mm. The composite shell is manufactured using unidirectional T300/epoxy laminates with a symmetric layup of $[45°/-45°/0°/0°/-45°/45°]$. Each lamina has a thickness of 0.04 mm. The corresponding mechanical properties of the lamina are listed in Table 2. Figs. 21c and 21d show the folding mechanism of the 4-meter-aperture antenna. Compared to the design for the 0.6-meter-aperture antenna, the folding mechanism here is slightly modified and consists of several key components. The central hub is responsible for wrapping the ribs; two side plates are installed to constrain the stowed volume of the antenna. The flanges are designed as straight plates and are connected to a circular shell that helps guide the local bending of the CTLT ribs. Finally, rollers are incorporated to facilitate rotational motion during folding. Membrane elements are used to discretize the reflector, composite shell elements are used for the CTLT ribs, and the folding mechanism components are modeled as rigid bodies. A mesh independence study was also conducted, and the final model includes 175168 membrane elements and 15360 shell elements per rib. The remaining simulation setup, including contact definitions and analysis procedures for the quasi-static folding and dynamic deployment analyses, is identical to that used for the 0.6-meter-aperture antenna.

5.2. Folding behavior

5.2.1. Folding of CTLT ribs

Fig. 22 illustrates the folding process of the parabolic CTLT ribs. As the folding progresses, all CTLT ribs are flattened and wrapped around the central hub, eventually stowed between the rollers and

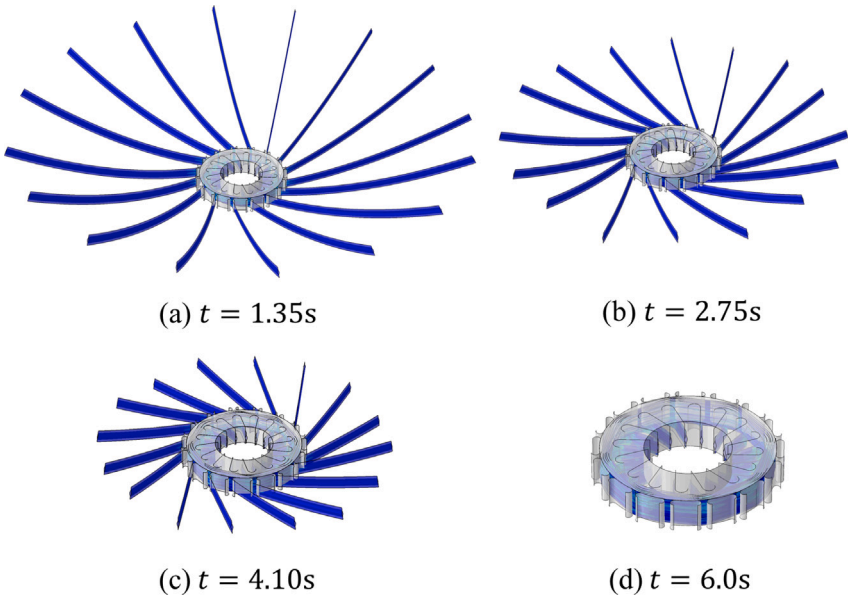

Fig. 22. Folding behavior of the parabolic CTLT ribs.

Table 2
Material properties of the unidirectional T300/epoxy lamina used in CTLT ribs.

Parameter	Description	Value
E_1	Axial modulus	131 GPa
E_2	Transverse modulus	5.89 GPa
G_{12}	In-plane shear modulus	3.5 GPa
G_{23}	Out-of-plane shear modulus	3.5 GPa
ν_{12}	In-plane Poisson's ratio	0.32
X_t	Axial tensile strength	1728 MPa
X_c	Axial compressive strength	1534 MPa
Y_t	Transverse tensile strength	98.8 MPa
Y_c	Transverse compressive strength	48.1 MPa
S_{12}	In-plane shear strength	107 MPa

flanges. Fig. 23 shows the fully stowed configuration, with contour plots indicating the distribution of the Tsai–Hill failure criterion. A comparative analysis was conducted for configurations with different numbers of CTLT ribs. The results indicate that, as the number of ribs increases, the stowed configuration becomes more compact, with the ribs experiencing greater compression. Nevertheless, the maximum Tsai–Hill index remains below 1.0 in all cases, indicating that the material remains within safe stress limits.

5.2.2. Folding of CTLT antenna

Fig. 24 shows the folding process of the 4-meter-aperture CTLT antenna with the reflector included. As the ribs are folded, the membrane automatically folds along with them. Throughout the process, the Tsai–Hill failure index remains below 1.0, indicating that the structure remains within safe stress limits.

5.3. Deployment behavior

Figs. 25 and 26 illustrate the deployment processes of the CTLT ribs and the complete CTLT antenna, respectively. Corresponding folding and deployment behaviors are shown in Videos S4 and S5 in the Supporting Materials. Similar to the 0.6-meter-aperture prototype, the ribs deploy in a dynamic manner. However, due to the presence of the membrane, the full antenna undergoes deployment with additional tension effect of the reflector.

The folding and deployment processes are also quantitatively characterized using the normalized parameters $H*$ and $R*$, with the corresponding results presented in Fig. 27. Figs. 27a and 27b present the evolution of the normalized parameters R^* and H^* throughout the folding and deployment processes. During folding, R^* decreases steadily from 1.0 to approximately 0.164, while H^* decreases from 1.0 to 0.083. Both parameters exhibit a similar trend: a gradual decrease in the initial phase, followed by a rapid change in the middle stage, and then a slower variation toward the end. This behavior is attributed to the quasi-static loading condition, implemented in ABAQUS using a smooth loading amplitude curve. During deployment, R^* increases more rapidly than H^* in the initial stage, suggesting that the antenna first expands radially before extending vertically. This sequential deployment behavior is consistent with observations from the high-speed video, as shown in Video S5 in the Supporting Materials. In addition, Fig. 27c shows the torque required for folding, as well as the reactive torque exerted by the antenna on the fixed constraint for deployment. Fig. 27d illustrates the evolution of strain energy: energy is gradually stored during folding and then rapidly released over a short duration during deployment.

6. Discussion and conclusions

This study presents a comprehensive investigation into the folding and deployment behavior of wrapped-rib antennas, with a focus on the mechanics of flexible parabolic ribs, membrane reflectors, and their coupled interactions. A 0.6-meter-aperture prototype was fabricated using C-shaped stainless steel ribs and a metallic mesh reflector. Through the development of a custom folding mechanism and dedicated experimental setups, key aspects of the folding and deployment processes were captured using torque measurements and high-speed imaging. High-fidelity finite element models were established to simulate the deformation and dynamic behavior of the structure, showing good agreement with experimental results.

The analysis was further extended to a 4-meter-aperture antenna employing composite thin-walled lenticular (CTLT) booms. The simulations demonstrated the feasibility of large-scale deployment while ensuring structural integrity, with Tsai–Hill failure indices remaining below critical thresholds. Parametric evaluations of deployment

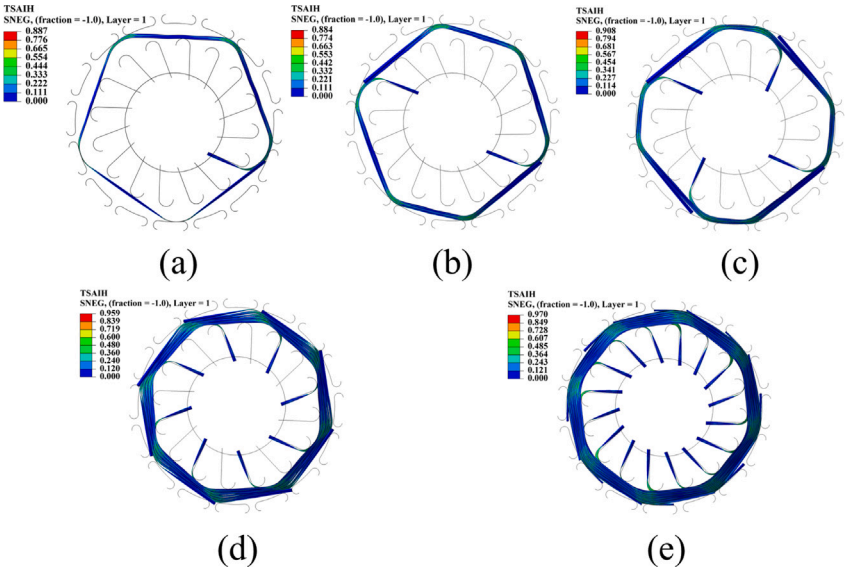

Fig. 23. Stowed configurations of multiple CTLT ribs with Tsai–Hill failure index distribution. (a) One rib. (b) Two ribs. (c) Four ribs. (d) Eight ribs. (e) Sixteen ribs.

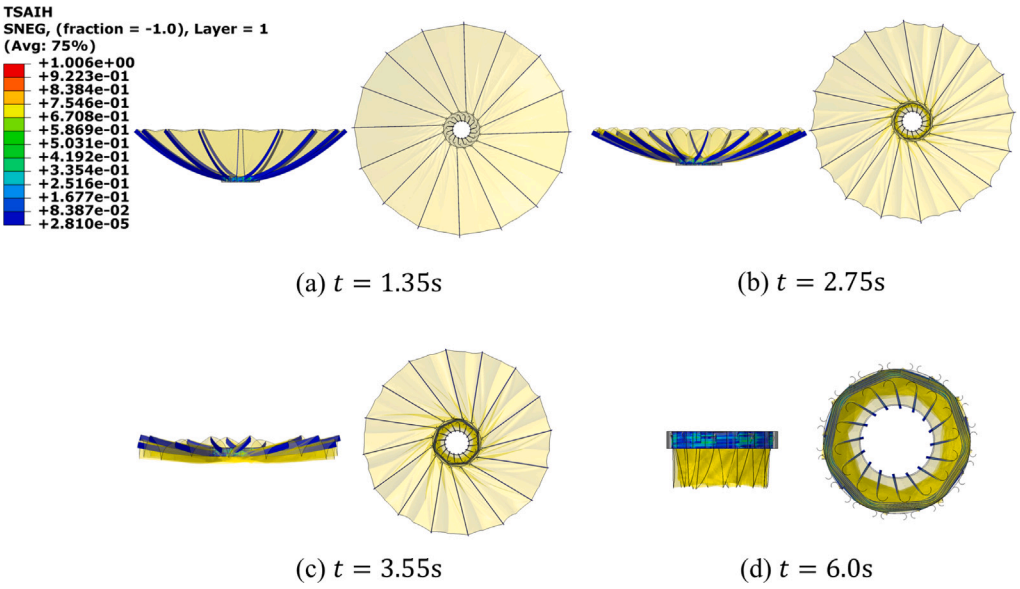

Fig. 24. Folding behavior of the 4-meter-aperture CTLT antenna.

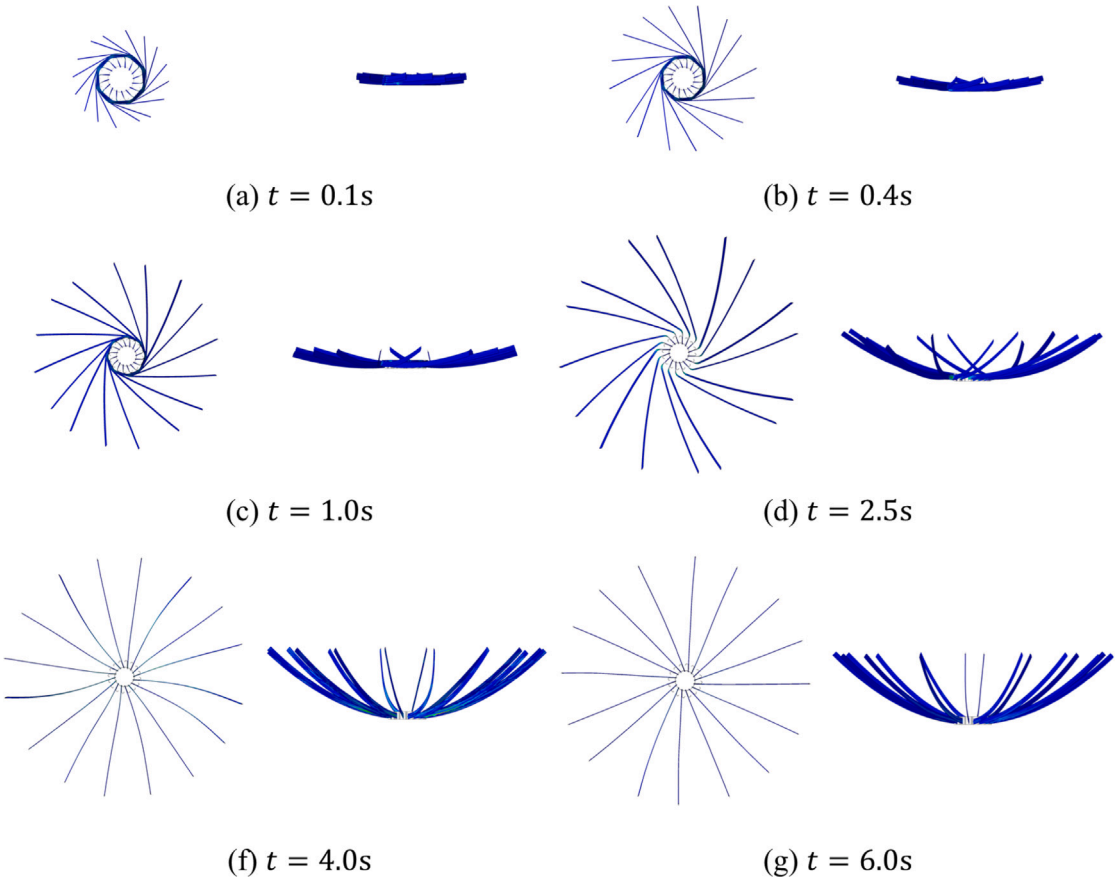

Fig. 25. Deployment behavior of the CTLT ribs.

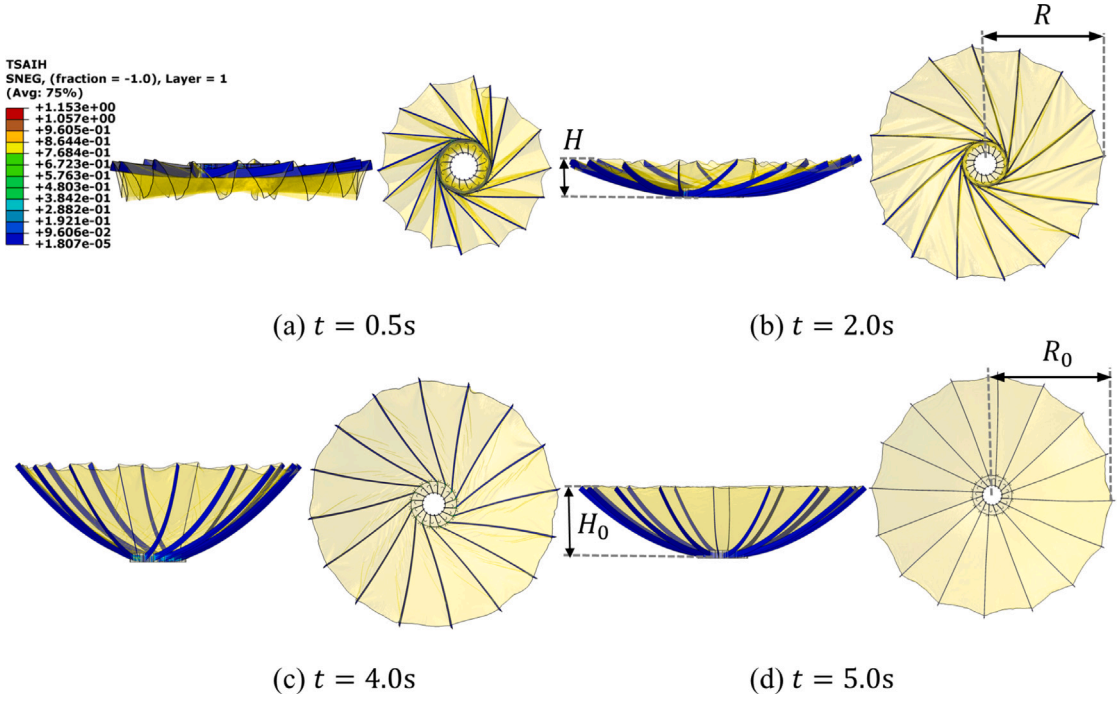

Fig. 26. Deployment behavior of the 4-meter-aperture CTLT antenna.

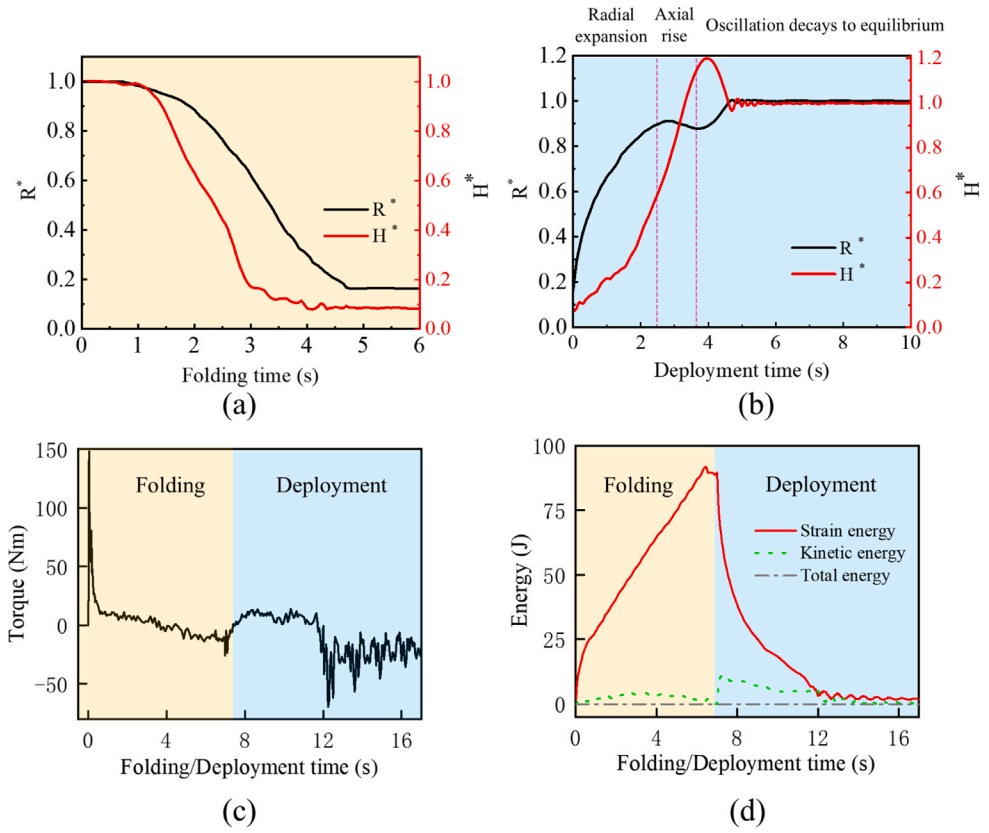

Fig. 27. Folding and deployment behavior of the 4-meter-aperture antenna. (a) Normalized height and radius of the antenna throughout the (a) folding and (b) deployment process. (c) Torque and (d) strain energy as a function of the folding and deployment process.

dynamics revealed a staged expansion behavior, characterized by initial radial growth followed by vertical extension—insights that were corroborated by experimental observations.

Overall, the present study provides design-relevant mechanical insight into the folding and deployment of thin-walled wrapped-rib antennas for potential space applications. The integrated experimental–numerical framework developed here is broadly transferable to other deployable systems combining flexible ribs with membrane components, and offers a validated basis for future design optimization of highly compact and low-complexity deployable space antenna.

Despite these contributions, several limitations remain due to experimental and modeling constraints. First, while we capture the wrapping torque evolution and deployment kinematics, the current test configuration does not yet provide a complete set of quantitative deployment metrics (e.g., synchronization error, transient contact/impact loads, and statistical repeatability over many cycles). Second, the present work does not aim to quantify the deployed surface accuracy. In our numerical model, the ribs and reflector are treated as ideal elastic bodies; under this assumption, the structure recovers its nominal geometry after release, and the deployed surface figure is primarily governed by the prescribed geometry and the membrane prestress (which can be established through standard form-finding, as discussed in previous works [17,38]). In practical hardware, however, surface accuracy may be degraded by non-idealities, including plasticity and accumulated damage under repeated folding–deployment cycles, manufacturing and assembly tolerances, hinge backlash, and frictional/contact hysteresis. Quantifying these effects requires dedicated surface metrology (e.g., photogrammetry or laser scanning) and systematic multi-cycle testing, and may further benefit from advanced material modeling that incorporates time- and history-dependent inelasticity (e.g., viscoelastic/viscoplastic deformation) of the ribs and membrane.

Future work will therefore (i) establish quantitative measurement protocols for deployment performance and repeatability, and (ii) couple surface-accuracy metrology with electromagnetic testing to determine how cycling history and non-ideal effects translate into surface error and RF performance.

CRediT authorship contribution statement

Shiran Zhu: Writing – original draft, Validation, Software, Methodology, Formal analysis, Data curation. **Ruiwen Guo:** Visualization, Methodology, Formal analysis, Data curation. **Haochen Liu:** Validation, Methodology, Formal analysis. **Xin Jin:** Resources, Conceptualization. **Xiaofei Ma:** Resources, Conceptualization. **Jinxiong Zhou:** Resources, Conceptualization. **Ning An:** Writing – review & editing, Writing – original draft, Resources, Methodology, Formal analysis, Conceptualization.

Declaration of competing interest

The authors declare that they have no known competing financial interests or personal relationships that could have appeared to influence the work reported in this paper.

Acknowledgments

This research is supported by the National Natural Science Foundation of China (grant 12202295), the International (Regional) Cooperation and Exchange Projects of the National Natural Science Foundation of China (grant W2421002), and the Sichuan Science and Technology Program (grant 2025ZNSFSC0845). Ning An gratefully acknowledges support from the China Scholarship Council (No. 202506240177). We also thank Prof. Pibo Ma of Jiangnan University for kindly providing the metallic mesh reflector used in fabricating the antenna prototype.

Appendix A. Supplementary data

Supplementary material related to this article can be found online at https://doi.org/10.1016/j.actaastro.2026.04.032.

Data availability

The raw experimental data and finite element simulation codes used to reproduce the results presented in this study are publicly available at: https://github.com/SCU-An-Group/Wrapped-rib-Antenna.

References

[1] Xiaofei Ma, Tuanjie Li, Jingya Ma, Zhiyi Wang, Chuang Shi, Shikun Zheng, Qifeng Cui, Xiao Li, Fan Liu, Hongwei Guo, et al., Recent advances in space-deployable structures in China, Engineering 17 (2022) 207–219.

[2] Xiaofei Ma, Ning An, Qiang Cong, Jiang-Bo Bai, Minger Wu, Yan Xu, Jinxiong Zhou, Dayu Zhang, Taotao Zhang, Ruiwen Guo, et al., Design, modeling, and manufacturing of high strain composites for space deployable structures, Commun. Eng. 3 (1) (2024) 78.

[3] Tian-Wei Liu, Jiang-Bo Bai, Nicholas Fantuzzi, Xiang Zhang, Thin-walled deployable composite structures: a review, Prog. Aerosp. Sci. 146 (2024) 100985.

[4] Mukesh Chandra, Satish Kumar, Somnath Chattopadhyaya, Sayan Chatterjee, Prakash Kumar, A review on developments of deployable membrane-based reflector antennas, Adv. Space Res. 68 (9) (2021) 3749–3764.

[5] Bing Wang, Juncheng Zhu, Shuncong Zhong, Wei Liang, Chenglong Guan, Space deployable mechanics: A review of structures and smart driving, Mater. Des. 237 (2024) 112557.

[6] E.V. Morozov, A.V. Lopatin, A.A. Khakhlenkova, Finite-element modelling, analysis and design of anisogrid composite lattice spoke of an umbrella-type deployable reflector of space antenna, Compos. Struct. 286 (2022) 115323.

[7] A.V. Lopatin, E.V. Morozov, Modal analysis of the thin-walled composite spoke of an umbrella-type deployable space antenna, Compos. Struct. 88 (1) (2009) 46–55.

[8] E.V. Morozov, A.V. Lopatin, A.V. Shatov, Z.A. Kazantsev, Composite anisogrid lattice toroidal shell: Application to a load-carrying rim of the spacecraft reflectarray antenna, Compos. Struct. 331 (2024) 117860.

[9] Rui Nie, Baiyan He, Shaoze Yan, Xiaofei Ma, Optimization design method for mesh reflector antennas considering the truss deformation and thermal effects, Eng. Struct. 208 (2020) 110253.

[10] Yutao Wang, Qian Zhang, Chao Jiang, Ahmad B.H. Kueh, Jian Feng, Jianguo Cai, Packing optimization and design of the deployable parabolic rigid antenna based on origami, Adv. Space Res. 73 (12) (2024) 6226–6240.

[11] Hao Jin, Qilong Jia, Ning An, Guiping Zhao, Xiaofei Ma, Jinxiong Zhou, Surrogate modeling accelerated shape optimization of deployable composite tape-spring hinges, AIAA J. 60 (10) (2022) 5942–5953.

[12] Jiang-Bo Bai, Fei-Yan You, Zhen-Zhou Wang, Nicholas Fantuzzi, Qing Liu, Hao-Tian Xi, Guang-Yu Bu, Yong-Bin Wang, Shi-Qing Wu, Rui Feng, et al., An efficient multi-objective optimization framework for thin-walled tubular deployable composite boom, Compos. Struct. 327 (2024) 117713.

[13] Bing Wang, Keith A. Seffen, Simon D. Guest, Tung-Lik Lee, Shi Huang, Shifeng Luo, Jiawei Mi, In-situ multiscale shear failure of a bistable composite tape-spring, Compos. Sci. Technol. 200 (2020) 108348.

[14] Pedro Fernandes, Ricardo Pinto, A. Ferrer, Nuno Correia, Performance analysis of a damage tolerant composite self-deployable elastic-hinge, Compos. Struct. 288 (2022) 115407.

[15] Katia N. Urata, Josaphat T. Sri Sumantyo, Cahya E. Santosa, Tor Viscor, A compact C-band CP-SAR microsatellite antenna for earth observation, Acta Astronaut. 159 (2019) 517–526.

[16] Ogi Yoshiro, Juan Reveles, Vincent Fraux, Dove-Jay Ashley, Deployable wrapped rib assembly, 2019, Google Patents, US Patent App. 16/348, 390.

[17] Di Wu, Minger Wu, Ping Xiang, Zhongxi Yan, Surface accuracy analysis and optimization design of rib-mesh paraboloidal antenna reflectors, Aerosp. Sci. Technol. 129 (2022) 107817.

[18] Han Zhang, Minger Wu, Ping Xiang, Di Wu, Zhongxi Yan, Qifeng Cui, Design, analysis, and test of an ultra-compact X-band deployable wrap-rib antenna, Acta Astronaut. 228 (2025) 918–930.

[19] A.V. Lopatin, E.V. Morozov, Z.A. Kazantsev, N.A. Berdnikova, Deployment analysis of a composite thin-walled toroidal rim with elastic hinges: Application to an umbrella-type reflector of spacecraft antenna, Compos. Struct. 306 (2023) 116566.

[20] Xiao Zhang, Rui Nie, Yan Chen, Baiyan He, Deployable structures: structural design and static/dynamic analysis, J. Elasticity 146 (2) (2021) 199–235.

[21] Jonathan Sauder, Christine Gebara, Narravula Harshavardhan Reddy, Carlos J. García-Mora, A framework for small satellite deployable structures and how to deploy them reliably, Commun. Eng. 3 (1) (2024) 72.

[22] Huizhong Zhang, Qian Zhang, Xiao Liang, Kuan Yao, Ahmad B.H. Kueh, Jianguo Cai, Rigidity analysis and mechanical properties of programmable origami tubes, Mech. Res. Commun. 132 (2023) 104182.

[23] Mehran Mobrem, Douglas S. Adams, Deployment analysis of the lenticular jointed antennas onboard the Mars express spacecraft, J. Spacecr. Rockets 46 (2) (2009) 394–402.

[24] Eric Ecale, Felice Torelli, Ignacio Tanco, JUICE interplanetary operations design: drivers and challenges, in: 2018 SpaceOps Conference, 2018, p. 2493.

[25] Tian-Wei Liu, Jiang-Bo Bai, Nicholas Fantuzzi, Guang-Yu Bu, Dong Li, Multi-objective optimisation designs for thin-walled deployable composite hinges using surrogate models and genetic algorithms, Compos. Struct. 280 (2022) 114757.

[26] ZhongYi Chu, YiAn Lei, Design theory and dynamic analysis of a deployable boom, Mech. Mach. Theory 71 (2014) 126–141.

[27] Jae Hyuk Lim, Yeong-Bae Kim, Ik-Soo Jang, Hongrae Kim, Hyun-Ung Oh, Parabolic deployable mesh antenna with a hingeless system of superelastic SMA ribs and composite tape springs, Acta Astronaut. 200 (2022) 149–162.

[28] Tian-Wei Liu, Jiang-Bo Bai, Nicholas Fantuzzi, Hao-Tian Xi, Hao Xu, Shao-Lin Li, Peng-Cheng Cao, Folding behavior of thin-walled tubular deployable composite boom for space applications: Experiments and numerical simulation, Acta Astronaut. 209 (2023) 159–171.

[29] Yu Hu, Wujun Chen, Ruixiong Li, Guangqiang Fang, Mechanical characteristics of deployable composite thin-walled lenticular tubes, Compos. Struct. 153 (2016) 601–613.

[30] Wujun Chen, Guangqiang Fang, Yu Hu, An experimental and numerical study of flattening and wrapping process of deployable composite thin-walled lenticular tubes, Thin-Walled Struct. 111 (2017) 38–47.

[31] Jiang-Bo Bai, Di Chen, Jun-Jiang Xiong, R. Ajit Shenoi, Folding analysis for thin-walled deployable composite boom, Acta Astronaut. 159 (2019) 622–636.

[32] Ruiwen Guo, Xin Jin, Qilong Jia, Xiaofei Ma, Ning An, Jinxiong Zhou, Folding, stowage, and deployment of composite thin-walled lenticular tubes, Acta Astronaut. 213 (2023) 567–577.

[33] Jinfeng Deng, Ning An, Qilong Jia, Xiaofei Ma, Deployment analysis of composite thin-walled lenticular tubes with effect of storage time and temperature, Chin. J. Aeronaut. 37 (1) (2024) 162–172.

[34] Zhongxi Yan, Minger Wu, Analysis and tests of non-uniform wrapping process of tape spring, Int. J. Solids Struct. 281 (2023) 112444.

[35] Fengyuan Liu, Minger Wu, Ping Xiang, Jae-Yeol Kim, Dynamic analysis of the uncoiling process of multiple tape springs, Thin-Walled Struct. 211 (2025) 113079.

[36] Zhi-Quan Liu, Hui Qiu, Xiao Li, Shu-Li Yang, Review of large spacecraft deployable membrane antenna structures, Chin. J. Mech. Eng. 30 (2017) 1447–1459.

[37] Shunji Zhang, Shuxin Zhang, Yiqun Zhang, Jing Ye, Force density sensitivity form-finding design method for cable-mesh reflector antennas considering interactive effects between cable network and supporting truss, Eng. Struct. 244 (2021) 112722.

[38] Shiran Zhu, Ruiwen Guo, Xin Jin, Xiaofei Ma, Jinxiong Zhou, Ning An, Form finding of cable-membrane structures with flexible frames: Finite element implementation and application to surface accuracy analysis of umbrella-like rib-mesh reflectors, Adv. Eng. Softw. 198 (2024) 103789.

[39] Jianguo Cai, Zheng Ren, Yifan Ding, Xiaowei Deng, Yixiang Xu, Jian Feng, Deployment simulation of foldable origami membrane structures, Aerosp. Sci. Technol. 67 (2017) 343–353.

[40] Chao Xie, Zhiyi Wang, Yu Liu, Feng Gao, Li Qin, Jinping Yang, Fujun Peng, Wujun Chen, Design and demonstration of a roll-out membrane antenna based on thin-walled deployable composite booms, Thin-Walled Struct. 205 (2024) 112486.

[41] Takumi Saito, Toshinori Kuwahara, Alperen Pala, Yasuyuki Miyazaki, Tetsuya Kaneko, FEM dynamic simulation technique for membrane structure deployment and model evaluation, Acta Astronaut. 218 (2024) 342–355.

[42] Tingting Yuan, Zhuyong Liu, Yuhang Zhou, Jinyang Liu, Dynamic modeling for foldable origami space membrane structure with contact-impact during deployment, Multibody Syst. Dyn. 50 (2020) 1–24.

[43] Zhuangzai Wu, Ping Xiang, Minger Wu, Chaozhe Niu, Fuling Guan, Design, analysis and testing of a 0.5 m diameter wrapped rib-tensioned surface reflector demonstrator, in: Proceedings of IASS Annual Symposia, vol. 2018, no. 14, International Association for Shell and Spatial Structures (IASS), 2018, pp. 1–5.

[44] Qilong Jia, Ning An, Xiaofei Ma, Jinxiong Zhou, A dynamic finite element procedure for bending collapse of composite thin-walled lenticular tubes, Compos. Struct. 287 (2022) 115364.

[45] Tian-Wei Liu, Jiang-Bo Bai, Nicholas Fantuzzi, New insights into folding tape-spring, Compos. Struct. 341 (2024) 118225.

[46] Tong Yang, Ping Yang, Zhuanyong Zou, Pibo Ma, Mechanical properties of warp-knitted metal mesh fabric under biaxial tension loading, Text. Res. J. 91 (11–12) (2021) 1368–1379.

[47] Qilong Jia, Ning An, Xiaofei Ma, Jinxiong Zhou, Exploring the design space for nonlinear buckling of composite thin-walled lenticular tubes under pure bending, Int. J. Mech. Sci. 207 (2021) 106661.